



# New findings on the evolution of the instability surface of loose sand

P. K. Triantafyllos<sup>1</sup> · V. N. Georgiannou<sup>1</sup> · Y. F. Dafalias<sup>2,3</sup> · I.-O. Georgopoulos<sup>2</sup>

Received: 27 January 2018 / Accepted: 16 November 2019 / Published online: 4 December 2019  
© Springer-Verlag GmbH Germany, part of Springer Nature 2019

## Abstract

The conditions that trigger the unrestrained flow deformation of loose anisotropic sand are investigated. An instability surface (IS) is defined in the deviatoric plane. It comprises the transient-peak states at which flow instability is triggered when isotropically consolidated sand is subjected to monotonic undrained loading at various fixed directions of principal stress,  $\alpha$ , under constant mean total stress,  $p$ , and fixed stress parameter,  $b = (\sigma'_2 - \sigma'_3)/(\sigma'_1 - \sigma'_3) = 0.5$ . Generalised undrained loading including rotation of the  $\sigma'_1$ -axis is also imposed on anisotropically consolidated sand. The mobilisation of the instability stress ratio,  $\sin \varphi_{ip} = (\sigma'_1 - \sigma'_3)/(\sigma'_1 + \sigma'_3)$ , that corresponds to stress direction  $\alpha$  via the IS locus, generally, triggers flow under loading with both fixed and rotating  $\sigma'_1$ -axis. Novel results are also presented: loose sand is subjected to undrained principal stress rotation at constant deviatoric stress, yet the previously established IS is crossed stably and flow is triggered after stress rotation is imposed on the failure surface, while a non-flow diffuse instability is triggered on the failure surface under increasing stresses and decreasing stress ratio. The experimental results indicate that the triggering of flow instability depends on the stress–strain history as well as on the incremental stress direction. It is also shown that both diffuse and localised instabilities occur preferably at stress states corresponding to unfavourable deformation kinematics.

**Keywords** Anisotropy · Flow deformation of sand · Instability · Principal stress rotation · Stress–strain history effects

## 1 Introduction

Flow deformation of loose saturated sands under monotonic undrained loading is exhibited as a strength drop after a transient peak, with concurrent accumulation of unidirectional shear strain and excess pore-water pressure [74]. Past the peak point, the deviatoric stress,  $q$ , decreases due to excess pore-water pressure build-up [60], while the effective stress ratio,  $\eta = q/p'$ , increases; that is, the material hardens during stress unloading [36]. Flow of sand masses in the field is actually an unstable behaviour since

large deformation is induced by small perturbations [33]; in laboratory testing, instability occurs if proper control parameters are chosen [7, 36, 68]. The triggering of flow instability results in a sudden transition from a quasi-static to a dynamic deformation mode, with a sharp increase in the strain rate, indicating the occurrence of bifurcation [14]. The non-uniqueness of the post-peak branches of the stress–strain curves (and stress paths) [11, 18] exposes another property of the bifurcated flow behaviour, namely the dependence on imperfections and perturbations in the system [77].

Recognising that flow deformation is an unstable bifurcated behaviour, some researchers applied the principles of stability and bifurcation theories to determine the flow instability condition. Lade et al. [36] reported that owing to the non-associative characteristics of sands, instability may occur along certain stress paths inside the failure surface, that is, before the peak stress ratio is mobilised. Lade and Pradel [37] showed that the condition of non-positive second-order work  $d^2W \leq 0$  (i.e. the violation of Hill's sufficient condition for stability [30]) is necessary for instability, among other requirements. Lade [38] defined a straight line in the  $q - p'$  plane that passes through the

✉ P. K. Triantafyllos  
ptriantafyllos@yahoo.com

<sup>1</sup> Department of Geotechnical Engineering, National Technical University of Athens, University Campus Zografou, Heroon Polytechniou 9, 15773 Zografou, Greece

<sup>2</sup> Department of Mechanics, National Technical University of Athens, University Campus Zografou, Heroon Polytechniou 9, 15773 Zografou, Greece

<sup>3</sup> Department of Civil and Environmental Engineering, University of California, Davis, CA 95616, USA

origin and connects the peak- $q$  points of a series of effective stress paths from monotonic undrained compression tests on loose sand consolidated isotropically at different confining stresses. He suggested that this “instability line” (IL) constitutes the lower boundary of the region of potential instability.

On the other hand, Darve and his colleagues [14, 15, 58] showed that Lade’s IL is neither an intrinsic concept nor the lower boundary of the potential instability region; the same conclusion is drawn based on the physical experiments of Chu et al. [9, 10]. In these studies, the so-called axisymmetric strain path testing showed that instabilities may be triggered at stress states below the IL if proper strain directions are excited, by relaxing the isochoric condition and imposing a dilatancy rate different than that corresponding to fully drained conditions [47]; flow instability of dense sand under drained loading was also observed, without any signs of strain localisation. Darve suggested that the methodology for detecting potentially unstable stress–strain states should be based on a directional analysis in the strain or stress space (similar to the one introduced by Gudehus [26]) since  $d^2W$  is a directional quantity, dependent on stress–strain history, and the non-positive sign of this quantity is the necessary condition for instability. Specifically, if at a given stress–strain state, reached after a given stress–strain history,  $d^2W$  becomes non-positive along one or more directions, then the state is reputed potentially unstable; however, the exposure of instability additionally requires properly chosen control parameters.

In some experimental studies, it is stated that the IL is the locus at which flow instability is triggered irrespective of the stress–strain history (consolidation and undrained loading history). Vaid and his colleagues [74, 75] reported that there exists a unique effective stress ratio (i.e. the slope of Lade’s IL) the mobilisation of which triggers flow under monotonic undrained triaxial compression irrespective of the void ratio (as far as loose sand is considered),  $e$ , consolidation stress,  $\sigma'_{3c}$ , and consolidation stress ratio,  $K_c = \sigma'_{3c}/\sigma'_{1c}$ . Vaid observed that the mobilisation of the same stress ratio triggers unidirectional flow under cyclic undrained triaxial loading irrespective of the value of  $K_c$  and  $q_{cyc}/2\sigma'_{3c}$  ( $q_{cyc}$  is the cyclic deviatoric stress amplitude). Georgiannou and her colleagues reported that, in torsional shear testing, the IL defined under monotonic undrained loading forms the boundary to a stable response under cyclic loading [21, 35].

Similar conclusions were drawn by Nakata et al. [49] and Sivathayalan and Vaid [67] who performed monotonic undrained loading tests in the hollow-cylinder apparatus (HCA). Loading of isotropically consolidated sands was imposed at various inclinations of the major principal

stress,  $\sigma'_1$ , with respect to the deposition direction (vertical), measured by angle  $\alpha$ , while the mean total stress,  $p$ , and intermediate principal stress parameter,  $b = (\sigma'_2 - \sigma'_3)/(\sigma'_1 - \sigma'_3)$ , were kept constant. It was found that flow is triggered at successively lower mobilised stress ratio  $\sin \varphi = (\sigma'_1 - \sigma'_3)/(\sigma'_1 + \sigma'_3)$  as the direction of the  $\sigma'_1$ -axis aligns towards the horizontal bedding plane; curve fitting to the instability combinations  $(\alpha, \varphi)_{ip}$  yielded a well-defined locus for a given value of  $b$ . The researchers changed the consolidation history from isotropic to anisotropic and performed loading tests with both rotating [49, 67] and fixed  $\sigma'_1$ -axis [67]. It was found that the mobilised  $\varphi$  at a given stress direction  $\alpha$  when flow is triggered does not depend on the consolidation stress ratio,  $K_c = \sigma'_3/\sigma'_1$ , or the stress history that precedes the mobilisation of the state  $(\alpha, \varphi)_{ip}$ .

The present experimental study investigates the anisotropic behaviour of loose sand under undrained generalised loading including principal stress rotation. It is queried whether the triggering of flow instability can be correlated with the crossing of a fixed surface in the stress space. For this purpose, an instability surface (IS) is defined in the deviatoric plane, as a generalisation of Lade’s IL, and compared with the local boundary surface (LBS) introduced by Symes et al. [68] and extended by Shibuya et al. [63–65]. The lack of intrinsic value (non-uniqueness) in the generalised IL concept is proved without relaxing the isochoric condition, and the role of the stress–strain history, including the effect of  $K_c$  and incremental stress direction, in the triggering of flow instability is highlighted. The stress–strain history effects on the flow behaviour of sand are indicated using a new flow parameter. Finally, this study shows that the inherent anisotropy of sand may affect the triggering of both diffuse and localised instabilities under principal stress rotation and proves that diffuse instability can be triggered on the failure surface under increasing stresses and decreasing stress ratio.

## 2 Testing procedure

This section describes the testing procedure and gives details concerning the apparatus, the tested material, the specimen preparation method and the applied stress paths.

### 2.1 Hollow-cylinder torsional shear apparatus

The hollow-cylinder torsional shear apparatus (HCA) of National Technical University of Athens (NTUA) [21] was upgraded and used in order to perform the generalised loading tests. Figure 1a shows the hollow-cylinder specimen and the applied boundary loads. The model specimen

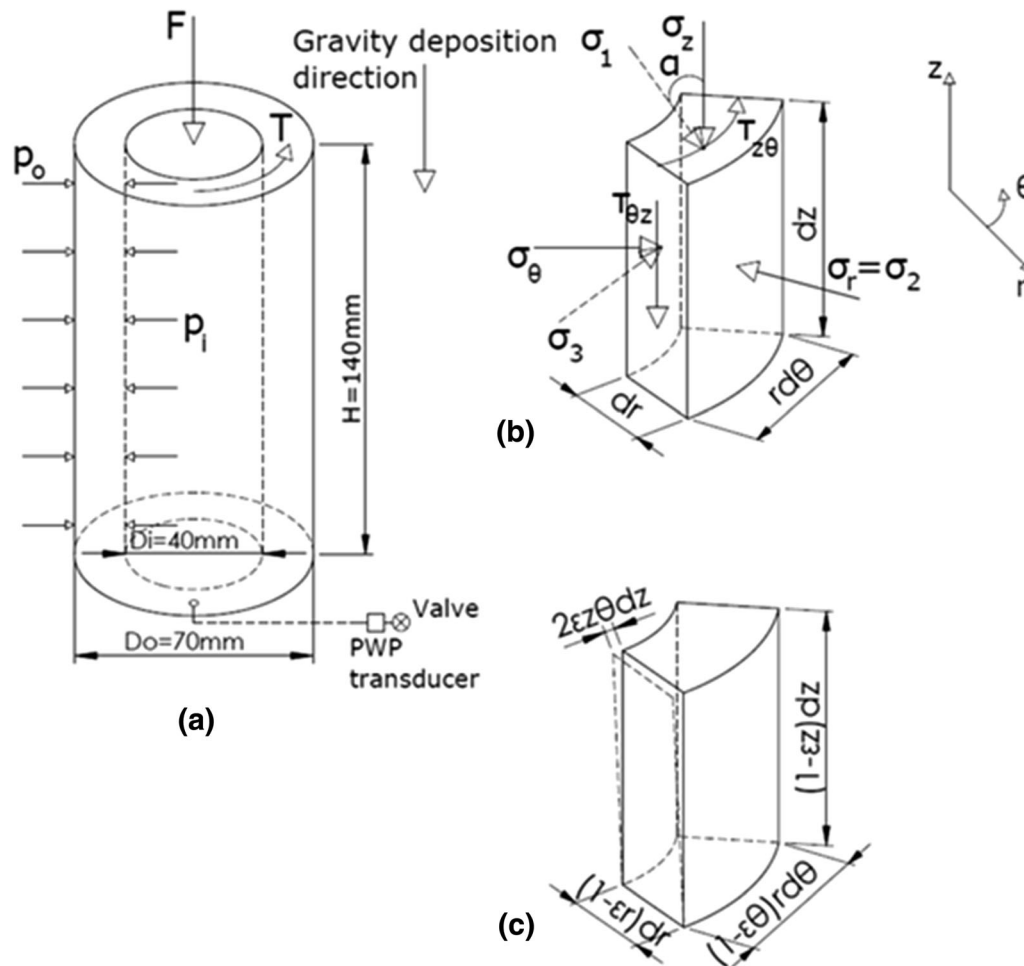


**Fig. 1** a Hollow-cylinder specimen and applied boundary loads. b Stress components on the undeformed soil element. c Deformed soil element under multiaxial and torsional strain components

has an initial inner radius,  $R_i$ , of 20 mm, outer radius,  $R_o$ , of 35 mm and height,  $H$ , of 140 mm, occupying an initial volume of  $V = 363$  cc. The usage of a small letter instead of a capital indicates the current value of the length dimension. The vertical load,  $F$ , torque,  $T$ , outer cell pressure,  $p_o$ , inner cell pressure,  $p_i$ , pore-water pressure,  $u$ , vertical displacement,  $v$ , torsional angle,  $\theta$ , and specimen volume change,  $\Delta V$ , are measured in time,  $t$ . The loading programme involves non-stiff control of the boundary stresses (by means of pneumatic pistons and flexible air-water interfaces away from the submerged membranes) under the isochoric (undrained) constraint to allow the occurrence of unrestrained flow deformation. High-frequency ( $f = 5$  Hz) data recording is generally used to capture efficiently the high-velocity flow response.

$F$  and  $T$  are measured internally (i.e. inside the triaxial cell), while the gravity and buoyancy forces acting upon the loading ram are counterbalanced automatically by the servo-mechanism control system.  $v$  is measured externally using a dial gauge, and  $\theta$  inside the cell at the top platen

using a potentiometer.  $\Delta V$  is measured by means of a burette equipped with a differential pressure transducer, allowing for the computation of global volumetric strain. The horizontal normal strains are computed by assuming  $\epsilon_{rr} = \epsilon_{\theta\theta}$ . In some cases, explicitly mentioned in the text, zero  $\epsilon_{rr}$  is assumed (plane strain deformation). Table 1 shows the equations used to calculate the average stresses, strains and other useful parameters [29, 48], while Fig. 1b, c shows the stresses applied to a soil element and the deformed soil element, respectively. Corrections for membrane restraint are applied, following the methodology proposed by Tatsuoka et al. [69].

## 2.2 Tested material and specimen preparation method

The uniform quartz M31 Sand was used for preparing the specimens; the grading curve of M31 Sand and the optical microscope image of the grains are shown in Fig. 2. The extreme void ratios ( $e_{\max}$ ,  $e_{\min}$ ), shape properties (aspect

**Table 1** List of symbols and equations used to calculate the average stresses, strains and other parameters

Direction HC	Stress	Strain
Vertical	$\sigma_{zz} = \frac{F}{\pi(r_o^2 - r_i^2)} + \frac{p_o r_o^2 - p_i r_i^2}{r_o^2 - r_i^2}$	$\varepsilon_{zz} = \frac{v}{H}$
Circumferential	$\sigma_{\theta\theta} = \frac{p_o r_o - p_i r_i}{r_o - r_i}$	$\varepsilon_{\theta\theta} = \frac{(\varepsilon_{vol} - \varepsilon_{zz})}{2}$ or $\varepsilon_{\theta\theta} = \varepsilon_{vol} - \varepsilon_{zz}$
Radial	$\sigma_{rr} = \frac{p_o r_o + p_i r_i}{r_o + r_i}$	$\varepsilon_{rr} = \frac{(\varepsilon_{vol} - \varepsilon_{zz})}{2}$ or $\varepsilon_{rr} = 0$
Rotational	$\tau_{z\theta} = \frac{3T}{2\pi(r_o^3 - r_i^3)}$	$\gamma_{z\theta} = 2\varepsilon_{z\theta} = \frac{2\theta(r_o^3 - r_i^3)}{3H(r_o^2 - r_i^2)}$
Principal	Stress	Strain
Major	$\sigma_1 = \frac{\sigma_{zz} + \sigma_{\theta\theta}}{2} + \sqrt{\left(\frac{\sigma_{zz} - \sigma_{\theta\theta}}{2}\right)^2 + \tau_{z\theta}^2}$	$\varepsilon_1 = \frac{\varepsilon_{zz} + \varepsilon_{\theta\theta}}{2} + \sqrt{\left(\frac{\varepsilon_{zz} - \varepsilon_{\theta\theta}}{2}\right)^2 + \varepsilon_{z\theta}^2}$
Intermediate	$\sigma_2 = \sigma_{rr}$	$\varepsilon_2 = \varepsilon_{rr}$
Minor	$\sigma_3 = \frac{\sigma_{zz} + \sigma_{\theta\theta}}{2} - \sqrt{\left(\frac{\sigma_{zz} - \sigma_{\theta\theta}}{2}\right)^2 + \tau_{z\theta}^2}$	$\varepsilon_3 = \frac{\varepsilon_{zz} + \varepsilon_{\theta\theta}}{2} - \sqrt{\left(\frac{\varepsilon_{zz} - \varepsilon_{\theta\theta}}{2}\right)^2 + \varepsilon_{z\theta}^2}$
Invariant	Stress	Strain
	$q = \left(\frac{1}{2} \left\{ (\sigma_1 - \sigma_2)^2 + (\sigma_2 - \sigma_3)^2 + (\sigma_3 - \sigma_1)^2 \right\}\right)^{1/2}$	$\gamma = \left(\frac{2}{9} \left\{ (\varepsilon_1 - \varepsilon_2)^2 + (\varepsilon_2 - \varepsilon_3)^2 + (\varepsilon_3 - \varepsilon_1)^2 \right\}\right)^{1/2}$
	$p' = \frac{\sigma'_1 + \sigma'_2 + \sigma'_3}{3} = \frac{\sigma_1 + \sigma_2 + \sigma_3}{3} - u$	$\varepsilon_{vol} = \varepsilon_1 + \varepsilon_2 + \varepsilon_3 (= \frac{\Delta V}{V})$
	$\tau_{oct} = \frac{1}{3} \left\{ (\sigma_1 - \sigma_2)^2 + (\sigma_2 - \sigma_3)^2 + (\sigma_3 - \sigma_1)^2 \right\}^{1/2}$	$\gamma_{oct} = \frac{2}{3} \left\{ (\varepsilon_1 - \varepsilon_2)^2 + (\varepsilon_2 - \varepsilon_3)^2 + (\varepsilon_3 - \varepsilon_1)^2 \right\}^{1/2}$
Parameters	Stress	Strain
Difference	$q_d = \sigma_1 - \sigma_3$ $X = \frac{\sigma'_{zz} - \sigma'_{\theta\theta}}{\sigma'_{zz} + \sigma'_{\theta\theta}}, X_s = \sigma'_{zz} - \sigma'_{\theta\theta}$ $\Upsilon = \frac{2\tau_{z\theta}}{\sigma'_{zz} + \sigma'_{\theta\theta}}, Y_s = 2\tau_{z\theta}$	$X_\varepsilon = \frac{\varepsilon_{zz} - \varepsilon_{\theta\theta}}{2}$ $Y_\varepsilon = \varepsilon_{z\theta}$
Major principal axis direction	$\alpha \equiv \alpha_{\sigma'_1} = 0.5 \cdot \tan^{-1} \frac{Y}{X} = 0.5 \cdot \tan^{-1} \frac{Y_s}{X_s}$	$\alpha_{\varepsilon 1} = 0.5 \cdot \tan^{-1} \frac{Y_\varepsilon}{X_\varepsilon}$
Major principal axis direction (for increments)	$\alpha_{d\sigma'_1} = 0.5 \cdot \tan^{-1} \frac{dY_s}{dX_s}$	$\alpha_{d\varepsilon 1} = 0.5 \cdot \tan^{-1} \frac{dY_\varepsilon}{dX_\varepsilon}$
Ratio	$b = \frac{\sigma'_2 - \sigma'_3}{\sigma'_1 - \sigma'_3}$	
Ratio	$\sin \varphi = \frac{\sigma'_1 - \sigma'_3}{\sigma'_1 + \sigma'_3}$	
Ratio	$\eta = \frac{q}{p'}$	
Ratio	$K_c = \frac{\sigma'_{3c}}{\sigma'_{1c}}$	
For isochoric conditions under $b = 0.5$	$d^2W = (d\sigma_{zz} - d\sigma_{\theta\theta}) \left( \frac{d\varepsilon_{zz} - d\varepsilon_{\theta\theta}}{2} \right) + 2d\tau_{z\theta}d\varepsilon_{z\theta}$ , for isochoric conditions under $b = 0.5$	
Angle between the $\sigma'_1$ -axis and the planes of $\max(\tau/\sigma'_n)$	$\theta_{1,2} = \pm(45^\circ - \varphi_{mob}/2)$	

ratio, sphericity and convexity), roughness and angularity of this sand are reported in [2] and [24]. In the present study, loose specimens with void ratio,  $e$ , between 0.710 and 0.730 were tested, while in some cases the value of  $e$  fell within the broader range of 0.695–0.745. (Details are given in Table 2.) Water-pluviated specimens were formed in order to achieve cross-anisotropic and homogeneous initial fabric characteristics [54, 76]. The homogeneity of void ratio over the specimen height was tested with a

methodology similar to the one reported in [76]. The sand specimen was stabilised using a dilute colloidal silica hydrosol [23] and cut up into three horizontal segments. The volume and dry sand mass of each segment were measured, and the corresponding void ratio was calculated. Table 3 shows the void ratio of each segment which was found to deviate only slightly from the average value corresponding to the entire specimen. However, it is recognised that the slightest void-ratio heterogeneity is

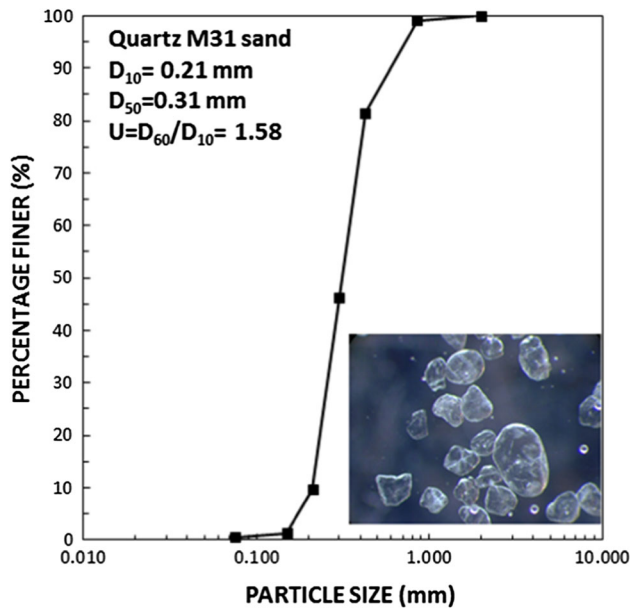


Fig. 2 Grading curve of M31 Sand and optical microscope image of grains

crucial concerning the triggering of instabilities [4, 78], while the heterogeneity may be larger than the reported here in a more local scale.

### 2.3 Consolidation and loading paths

The effective stress paths (ESPs) from the tests performed herein are plotted in both the  $q_d - p'$  (Fig. 3a) and deviatoric (Fig. 3b) planes. It is noted that the deviatoric plane (DP) is physically related to the torsional shear loading paths and differs from the octahedral plane. The coordinates  $X = (\sigma'_{zz} - \sigma'_{\theta\theta})/(\sigma'_{zz} + \sigma'_{\theta\theta})$  and  $Y = 2\tau_{z\theta}/(\sigma'_{zz} + \sigma'_{\theta\theta})$  correspond to the triaxial and torsional shear loading mode, respectively, with the numerators  $X_s = (\sigma'_{zz} - \sigma'_{\theta\theta})$ ,  $Y_s = 2\tau_{z\theta}$  controlled independently during undrained loading [32]. The ratios  $Y/X$  (or  $Y_s/X_s$ ) and  $dY_s/dX_s$  equal  $\tan 2\alpha_{\sigma_1}$  ( $\alpha_{\sigma_1} \equiv \alpha$  is the angle of  $\sigma'_1$  to the vertical; Fig. 1b) and  $\tan 2\alpha_{d\sigma_1}$  ( $\alpha_{d\sigma_1}$  is the angle of  $d\sigma'_1$  to the vertical), respectively, while the radial coordinate  $(X^2 + Y^2)^{1/2}$  equals the mobilised stress ratio  $\sin \varphi = (\sigma'_1 - \sigma'_3)/(\sigma'_1 + \sigma'_3)$ , as shown in Fig. 3b. It is noted that the direction of incremental stress in the  $Y-X$  plane, indicated by the angle  $\alpha_{ds}$  in Fig. 3b, provides information concerning the change in  $\alpha_{\sigma_1}$  and  $\sin \varphi$ , but it does not necessarily coincide with the direction of  $d\sigma'_1$ . The convention for the sign of direction angles is the same as the one used by Miura et al. [48].

After the saturation process is completed (yielding a coefficient  $B = du/dp > 0.96$ , at  $u = 300$  kPa), the specimens are consolidated either isotropically (IC), in the case of A-series tests (with some exceptions discussed next), or

anisotropically (AC), in the case of B- and C-series tests. Anisotropic consolidation, with duration of around 120 min, is performed in two phases, each followed by a creep period. During the first phase,  $p'$  increases from 40 kPa to  $p'_c$  under constant  $\eta = q/p'$  and  $K_c = \sigma'_{3c}/\sigma'_{1c}$ , and fixed  $\alpha = 0^\circ$  and  $b = 0$ . During the second phase,  $p'$  increases from  $p'_c$  to  $p'_i$  under constant  $\sigma'_{3c}$  and  $\sigma'_{1c}$ , fixed  $\alpha = 0^\circ$ , decreasing  $\eta$  and increasing  $\sigma'_2$  until the value of  $b = 0.5$  is reached. The compressibility and creep are more intense during the second phase in which the horizontal direction is compressed (and  $b$  is changed), indicating that the fabric is anisotropic at the end of anisotropic consolidation [79, 85]; the ratio of axial to volumetric strain, being considerably lower than 1/3, indicates that the same holds true at the end of isotropic consolidation.

The consolidation stress,  $p'_c$ , generally equals 200 kPa; the value of  $p'_c = 100$  kPa is imposed in tests A24–26 and B6–7. Specimen A23 is anisotropically consolidated at  $K_c = 0.5$ , while specimens A1, A3, A4 and A6 are isotropically consolidated and then subjected to drained pre-shearing by increasing the stress  $q$  under constant  $p'$  and  $b = 0.5$  until the value of  $\eta = 0.13$  ( $K_c = 0.86$ ) is reached. A drained rotation of the  $\sigma'_1$ -axis under constant  $\sigma'_1$ ,  $\sigma'_2$  and  $\sigma'_3$  is performed next at  $\eta = 0.13$  until the value of  $\alpha$  required for the subsequent undrained loading is reached. The volumetric strain accumulated during pre-shearing is minor ( $< 0.02\%$ ) due to the low value of  $\eta$ . The specimens in B-series tests are consolidated at  $K_c = 0.8, 0.5$  and  $0.4$ , while the specimens in C-series tests at  $K_c = 0.48$ – $0.75$ . Details concerning the consolidation are given in Table 2.

Three different undrained loading histories are imposed under constant  $p = p_i$  with a fixed value of  $b = 0.5$ . Monotonic loading is imposed on A-series tests by increasing  $q$  with a fixed value of  $\alpha$ , while in B-series tests, by simultaneously increasing  $q$  and  $\alpha$ ; in the latter case, stress rotation is performed continuously. In physical terms,  $\sigma_{zz}$  and  $\sigma_{\theta\theta}$  are changed in opposite trends in A-series tests to increase the difference  $(\sigma_{zz} - \sigma_{\theta\theta})$  and maintain the half-sum  $(\sigma_{zz} + \sigma_{\theta\theta})/2$  constant and equal to  $\sigma_{rr}$ , while  $\tau_{z\theta}$  is increased to maintain the ratio  $2\tau_{z\theta}/(\sigma_{zz} - \sigma_{\theta\theta})$  constant and equal to  $\tan 2\alpha$ . In B-series tests,  $\tau_{z\theta}$  is increased, while the other stresses are maintained constant. In C-series tests, the  $\sigma'_1$ -axis is rotated monotonically under constant values of  $\sigma_1$ ,  $\sigma_2$  and  $\sigma_3$  inducing an increase in  $u$  and  $\eta$  [49, 67, 68, 81]; this situation corresponds to isotropic unloading in the  $\sigma'_1 - \sigma'_2 - \sigma'_3$  space ( $d\sigma'_1 = d\sigma'_2 = d\sigma'_3 = -du < 0$ ). Physically, this is achieved by changing sinusoidally the stresses  $\sigma_{zz}$ ,  $\sigma_{\theta\theta}$ ,  $\tau_{z\theta}$  with a proper phase difference, while keeping  $\sigma_{rr}$  constant [49]. Stress rotation is performed stepwise, and the creep behaviour is observed during the short-time ( $\approx 2$  min)

**Table 2** Details of loading tests

Test	$\alpha$ (°)	$b$ (–)	$e_i$ (–)	$p'_i$ (kPa)	$K_c$ (–)	$\alpha_{ip}$ (°)	$b_{ip}$ (–)	$\phi_{ip}$ (°)	$\gamma_{oct,ip}$ (%)	$\tau_{oct,ip}$ (kPa)	$\Delta u_{ip}/p'_i$ (–)
A1	0	0.5	0.737	199	1.00/0.86	0.0	0.51	31.2	0.43	58.4	0.30
A2	10	0.5	0.716	199	1.00	9.8	0.52	35.9	0.49	66.5	0.29
A3	15	0.5	0.726	200	1.00/0.86	15.0	0.50	31.7	0.47	59.9	0.30
A4	22.5	0.5	0.719	199	1.00/0.86	22.3	0.51	29.9	0.50	55.6	0.31
A5	22.5	0.5	0.706	200	1.00	22.3	0.50	31.9	0.48	61.1	0.29
A6	30	0.5	0.717	199	1.00/0.86	29.9	0.51	28.0	0.49	53.1	0.30
A7	40	0.5	0.721	199	1.00	39.7	0.50	24.1	0.44	45.8	0.31
A8	45	0.5	0.727	199	1.00	44.7	0.50	22.3	0.38	44.0	0.29
A9	45	0.5	0.707	200	1.00	44.9	0.49	23.8	0.36	46.1	0.30
A10	45	0.5	0.745	199	1.00	44.9	0.50	19.7	0.32	38.7	0.29
A11	50	0.5	0.699	199	1.00	49.5	0.50	23.5	0.37	45.1	0.31
A12	60	0.5	0.719	199	1.00	59.3	0.51	20.5	0.23	39.7	0.30
A13	60	0.5	0.719	200	1.00	59.3	0.51	20.0	0.24	34.8	0.37
A14	67.5	0.5	0.712	199	1.00	68.9	0.51	18.8	0.27	34.7	0.33
A15	75	0.5	0.706	199	1.00	74.2	0.51	20.6	0.20	42.4	0.25
A16	75	0.5	0.717	199	1.00	74.0	0.51	18.4	0.24	33.7	0.34
A17	80	0.5	0.727	198	1.00	79.1	0.50	17.8	0.27	32.8	0.34
A18	67.5 <sup>a</sup>	0.5	0.714	199	1.00	62.5	0.50	20.0	0.30	39.0	0.31
A19	90	0.5	0.727	199	1.00	89.8	0.51	19.1	0.31	34.1	0.35
A20	90	0.5	0.714	200	1.00	89.6	0.52	19.7	0.31	36.7	0.32
A21	0	0	0.709	200	1.00	0.0	0.00	25.0	0.89	72.5	0.47
A22	90	1	0.697	200	1.00	90.0	1.00	16.3	0.16	33.7	0.18
A23	90	1	0.718	200	0.50	90.0	1.00	15.7	0.42	23.1	0.17
A24	30	0.5	0.726	99	1.00	29.4	0.51	27.4	0.31	26.5	0.28
A25	45	0.5	0.734	99	1.00	44.0	0.52	20.8	0.31	20.0	0.30
A26	80	0.5	0.717	100	1.00	79.3	0.52	17.7	0.22	16.3	0.34
B1	R0+	0.5	0.727	207	0.80	34.1	0.50	24.0	0.39	50.6	0.26
B2	R0+	0.5	0.711	223	0.50	19.1	0.50	32.7	0.40	78.3	0.20
B3	R0+	0.5	0.728	232	0.40	12.6	0.50	34.0	0.16	89.6	0.15
B4	R0+	0.5	0.711	206	0.80	34.4	0.51	24.9	0.33	54.4	0.23
B5	R0+	0.5	0.696	224	0.50	18.5	0.50	32.1	0.45	78.4	0.19
B6	R0+	0.5	0.701	111	0.50	20.7	0.51	33.1	0.40	41.0	0.17
B7	R0+	0.5	0.727	115	0.40	14.0	0.50	35.2	0.17	46.0	0.15
C1	R0+	0.5	0.730	225	0.48	26.3	0.51	29.3	0.40	64.7	0.28
C2	R0+	0.5	0.721	214	0.66	79.6	0.51	19.8	0.42	35.3	0.40
C3	R0+	0.5	0.721	209	0.75	57.4	0.51	25.6	0.45	23.7	0.68
C4	R0+	0.5	0.716	210	0.72	90.0	0.51	20.3	0.40	27.1	0.55
C5	R0+	0.5	0.713	212	0.70	79.6	0.51	23.4	0.50	30.9	0.55
C6	R0+	0.5	0.704	216	0.64	64.4	0.50	39.1	6.57	34.5	0.69
D1	R0+	.4–.5	0.738	211	0.70	– 85.5	0.40	21.9	0.33	23.2	0.67

<sup>a</sup>Loading at fixed stress direction  $\alpha_{\sigma'_1} = 67.5^\circ$  was followed by loading at fixed incremental stress direction  $\alpha_{d\sigma'_1} = 45^\circ$ . Index “i”, for initial, “c”, for consolidation and “ip”, for instability point

pause periods. It is noted that one conventional triaxial compression test (A21) and two conventional triaxial extension tests (A22 and A23) are also included in A-series tests, while in test A18, loading is imposed initially at a

fixed stress direction  $\alpha = 67.5^\circ$  (with  $b = 0.5$ ) that is changed before the triggering of instability, by increasing the stress  $\tau_{z\theta}$  and freezing the other stresses ( $\alpha_{d\sigma'_1} = 45^\circ$ ).

**Table 3** Results from the void-ratio homogeneity test over the specimen height

Segment	Position	Volume $V_i$ of ith segment in % of total volume $V_{tot}$	Void ratio $e_i$ of ith segment	Deviation $e_i - e_{av}$ in local void ratio from overall average void ratio <sup>a</sup>
1	Upper	32.9	0.715	- 0.003
2	Middle	35.4	0.717	- 0.001
3	Lower	31.7	0.722	0.004

<sup>a</sup>The overall average void ratio,  $e_{av} = 0.718$ , is calculated as  $e_{av} = \sum(e_i * V_i) / V_{tot}$ , where  $V_{tot} = \sum V_i$

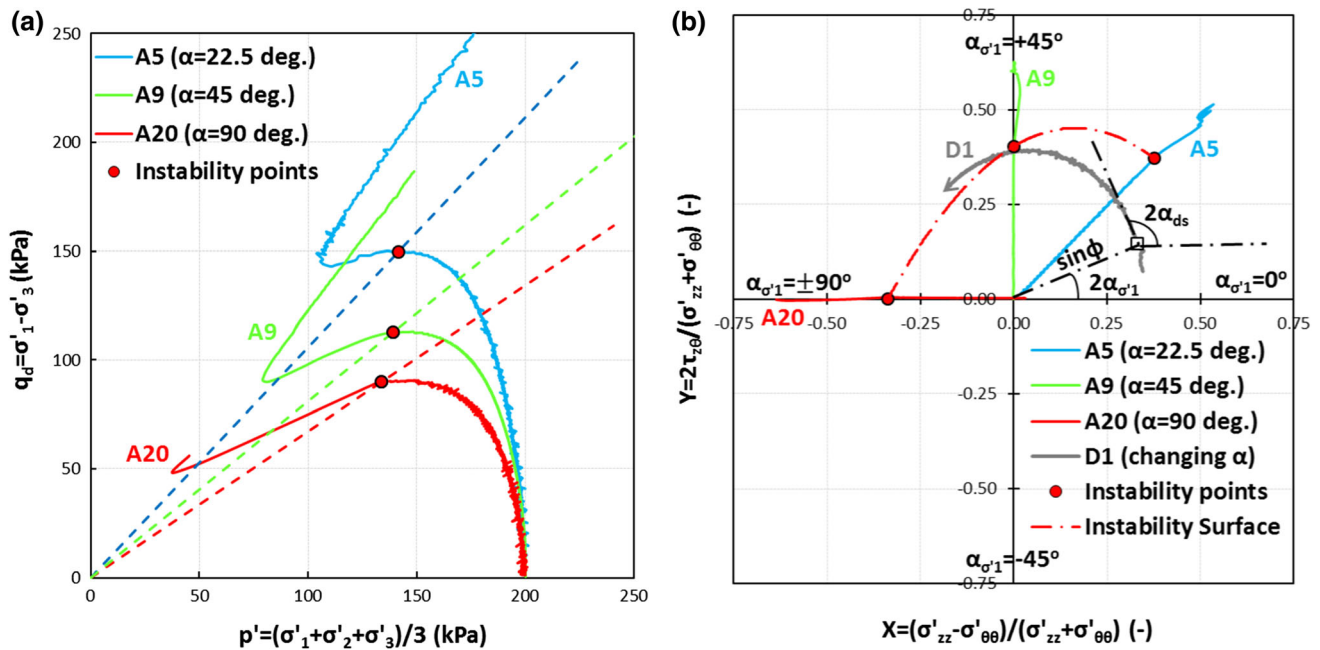


**Fig. 3** Definition of the local boundary surface [63, 68], instability lines [38] and instability surface (present study) of loose isotropically consolidated sand by means of effective stress paths **a** in the  $q_d - p'$  plane and **b** in the  $Y-X$  plane

### 3 Definitions of the local boundary surface and instability surface

Symes et al. [68] and Shibuya et al. [63–65] suggested that the set of ESPs from monotonic undrained loading tests with various fixed values of  $\alpha$  and  $b$ , and constant  $p$ , forms the local boundary surface (LBS) in the  $q_d - p' - \alpha - b$  space ( $q_d$  is the stress difference  $\sigma_1 - \sigma_3$ ). It was shown that the LBS bounds the effective stress space occupied by monotonic or cyclic undrained stress paths, with fixed or rotating  $\sigma'_1$ -axis. Moreover, it was shown that flow instability is triggered under stress-controlled undrained conditions when the ESP probes the post-peak regime of the LBS with an outwards direction. Similar results were reported by other researchers [1, 20].

The shape of the LBS is anisotropic and depends on the void ratio,  $e$ , of sand and consolidation stress history. According to Symes and Shibuya, this shape expresses

phenomenologically the initial anisotropy of sand (when  $\gamma_{oct} \ll 1\%$ ) resulting from the process of deposition of non-spherical or spherical grains (i.e. the inherent anisotropy; [5, 53, 63]) as well as from the consolidation stress history. However, the initial anisotropy is altered gradually as the sand is sheared to failure and beyond [55], and this effect of induced anisotropy cannot be observed separately when the LBS is determined. It should be noted that the quantification of fabric anisotropy (inherent, initial or induced) requires physical or numerical techniques [3, 55, 82] that are not included in this study. Figure 3a shows with solid lines the projection of the LBS on the  $q_d - p'$  plane for three different values of  $\alpha$  and  $b = 0.5$ ; these lines are actually the ESPs from A-series tests performed in this study.

The solid circles in Fig. 3a represent the instability points (IPs), while the broken lines connecting these points with the origin of stress space are, practically, the ILs in

Lade's sense. Instability is triggered at, or just after, the transient-peak state since the sand specimen cannot sustain the applied stresses, the strength declines and a runaway deformation occurs. At the instability state  $dq = 0$  while the development of strains (and excess pore-water pressure) is accelerated; thus, the controllability of the loading programme is lost [52]. Strength, stability and control are regained when flow is terminated at the phase transformation point (PTP) [31], which practically coincides with the minimum-strength point in this study. It is noted that for a given  $e$  and  $p'_i$  there exist different ILs for different values of  $\alpha$  (and  $b = 0.5$ ) due to the initial anisotropy of sand [49]. Each IL corresponds to a mobilised stress ratio  $\sin \varphi_{ip} = (\sigma'_1 - \sigma'_3)/(\sigma'_1 + \sigma'_3)$  that generally becomes lower when  $\alpha$  increases.

The instability surface (IS) in the deviatoric plane shown with broken line in Fig. 3b is introduced here as a generalisation of Lade's concept: it consists of the combinations ( $\sin \varphi_{ip}, 2\alpha$ ) in polar coordinates that correspond to the IPs (solid circles) observed in A-series tests. Shearing up to the IP is not expected to alter drastically the initial anisotropy of sand since the effective stress ratio and shear strain are low, and neither phase transformation nor failure has occurred; studies in which fabric anisotropy is quantified support this suggestion [55, 82]. Thus, it is postulated herein that the shape of the IS expresses phenomenologically the initial anisotropy of sand.

## 4 Experimental results and observations

The experimental results from the loading tests performed herein are presented and interpreted in this section.

### 4.1 Undrained behaviour of loose IC sand under monotonic loading with fixed stress principal axes: determination of the initial instability surface

The first series of loading tests (A-series) aims at the investigation of the undrained behaviour of loose IC M31 Sand under monotonic loading with fixed stress principal axes (PA) and determination of the IS. Figure 4a shows the ESPs in the  $q_d - p'$  plane from loading tests at various fixed stress directions  $\alpha$  under  $b = 0.5$  and constant  $p$ ; the solid circles at or near the transient-peak states indicate the IPs. Figure 4b shows the corresponding octahedral shear stress–strain curves for  $\gamma_{oct}$  only up to 8%. Strain localisation is not observed with naked-eye inspection up to the termination of flow (at the PTP); instead, the deformation is of the diffuse mode [18, 36]. However, localised deformation in loose sands is reported in [17, 19] and is

observed herein beyond  $\gamma_{oct} = 8\%$ . The results presented in Fig. 4 were obtained from tests on specimens consolidated to stress  $p'_c = 200$  kPa ( $= p'_i$ ), having initial void ratio  $e_{i-} = 0.707\text{--}0.719$ , except from specimen A3, which had  $e_i = 0.726$ .

The results in Fig. 4a, b indicate that loose water-pluviated IC sand is highly anisotropic. The sand's behaviour becomes generally more contractive and less stiff when  $\alpha$  increases exhibiting lower peak- $q_d$  and minimum- $q_d$  strengths, while the excess pore-water pressure and shear strain accumulated at the PTP are higher; similar results are reported in [83]. However, the weakest response is exhibited at stress directions between  $\alpha = 60^\circ$  and  $\alpha = 75^\circ$ . This behaviour is frequently attributed to shearing along the bedding plane when one of the planes of maximum stress obliquity aligns with it [39, 48, 49, 54, 70]; deformation in this situation may be diffuse or localised. The effect of uncontrollable stress rotation during flow in tests A14 and A16, discussed in Sects. 4.2 and 5, should be also considered herein.

Figure 5 shows the IPs in the deviatoric plane, from all A-series tests with  $p'_i = 200$  kPa and  $b = 0.5$ , as solid or hollow circles for loose or very loose sand, respectively, together with their reflections in the negative- $Y$  regime; results from A-series tests at different  $p'_i$  or  $b$  are given in Table 2. Curve fitting to the IPs yields the so-called initial instability surface, the shape of which is postulated to express phenomenologically the initial anisotropy of loose IC M31 Sand. The IS is a part of an ellipse symmetric about the X-axis, having its minor axis parallel to the Y-axis at  $X > 0$ . During the course of instability, the sand exhibits plastic deformation [10, 36]; however, the IS is neither a yield nor a plastic potential surface; for example, it is open at  $\alpha < 10^\circ$  because loose M31 Sand is stable when loaded normal to the bedding plane. The IS is the generalisation of Lade's IL; thus, it is not the lower boundary of the region of potential instability.

The unit vectors shown in Fig. 5 indicate the direction  $\alpha_{de1}$  of the major principal strain increment when instability is triggered.  $\alpha_{de1}$  is determined using the incremental relationship listed in Table 1 for two neighbouring states, near the IP, in the  $X_e - Y_e$  strain space, under the assumption of  $\varepsilon_{rr} = \varepsilon_{\theta\theta}$ ; it is noted that the corresponding stress increment in the  $X_s - Y_s$  stress space is radial ( $\alpha_{d\sigma 1} = \alpha_{\sigma 1}$ ). It can be inferred that the sand behaviour under radial (fixed- $\alpha$ ) loading is non-coaxial since the angle difference  $\alpha_{de1} - \alpha_{\sigma 1}$  is nonzero; similar results are obtained if  $\varepsilon_{rr} = 0$ . The vectors deviate, in general, from the radial direction towards the Y-axis when superimposed on the instability stress states, with the deviation being larger at around  $\alpha = 22.5^\circ$  and  $75^\circ$ . Miura et al. [48] and Gutierrez et al.



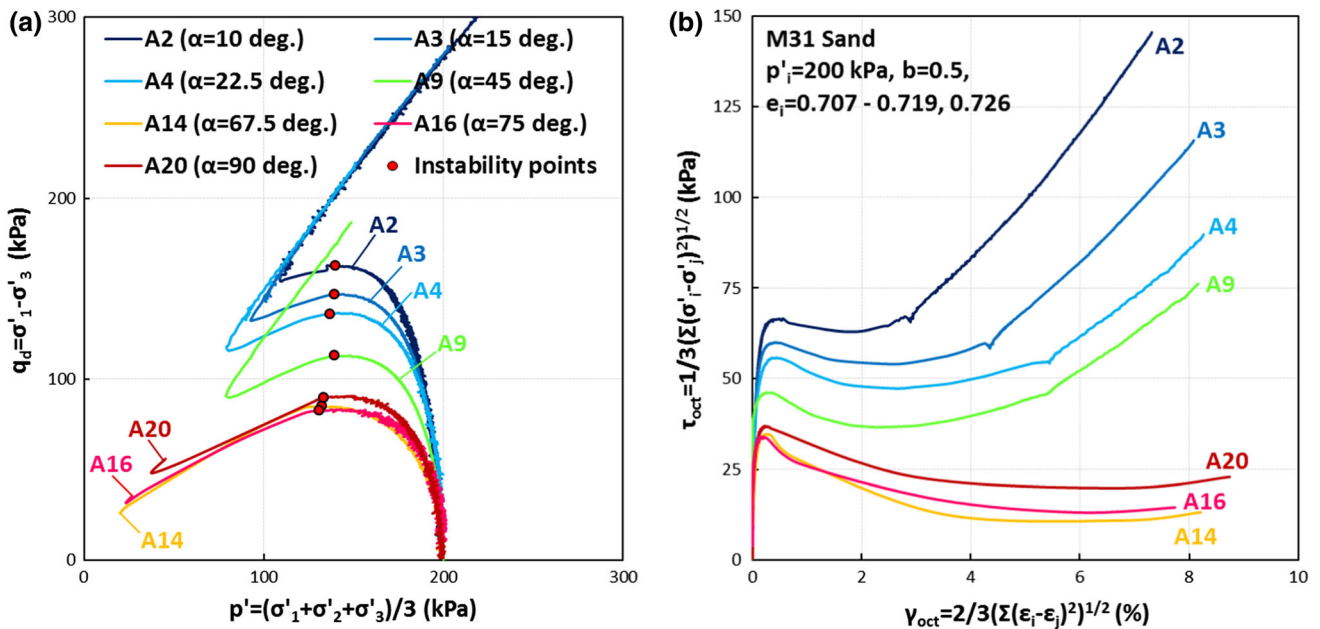


Fig. 4 Response of loose isotropically consolidated sand to monotonic undrained loading with fixed stress principal axes. a Stress paths in the  $q_d - p'$  plane. b Stress–strain curves in the  $\tau_{oct} - \gamma_{oct}$  plane

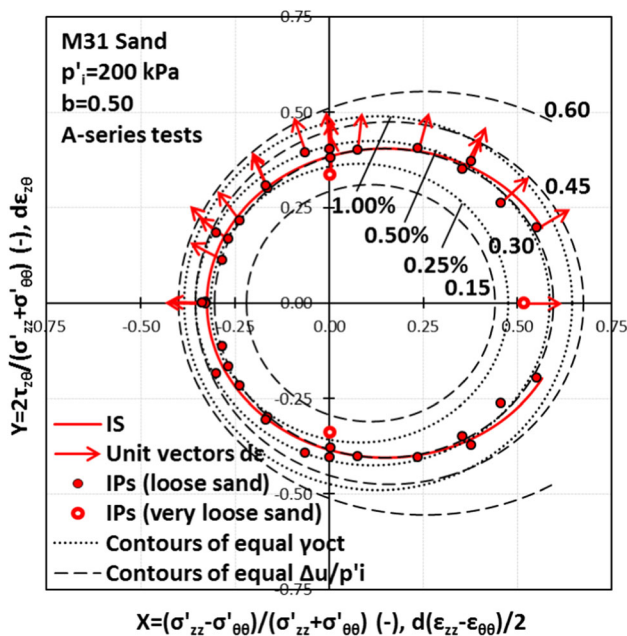


Fig. 5 Instability surface of loose isotropically consolidated sand and contours of equal  $\gamma_{oct}$  and  $\Delta u/p'_i$  in the  $Y-X$  plane

[28] reported a similar behaviour, and the former authors suggested that it is due to the initial anisotropy of sand.

Figure 5 also shows the contours of equal shear strain  $\gamma_{oct}$  (0.25%, 0.50% and 1.00%; dotted lines) and normalised excess pore-water pressure  $\Delta u/p'_i$  (0.15, 0.30, 0.45 and 0.60; dashed lines) at contractant states in the  $Y-X$  plane together with the IS (solid line). The contours are ellipses symmetric about the  $X$ -axis, having their minor

axis parallel to the  $Y$ -axis at  $X > 0$ ; the contour  $\Delta u/p'_i = 0.60$  is open at one end because the maximum  $\Delta u/p'_i$  developed when  $\alpha < 20^\circ$  is lower than 0.60. The deformability of sand is apparently anisotropic: the stress ratio corresponding to a particular value of  $\gamma_{oct}$  or  $\Delta u/p'_i$  decreases significantly with  $\alpha$ . The value of  $\gamma_{oct}$  at the IP is around 0.50% in the compression regime and shifts gradually to 0.25% in the extension regime, while an essentially constant value of  $\Delta u/p'_i = 0.30$  is observed irrespective of  $\alpha$  and  $e$  (see also Table 2). Similar results are reported in [33, 49].

#### 4.2 Undrained behaviour of loose AC sand under monotonic loading with rotating stress principal axes: triggering of flow on the initial instability surface

The results from B-series (B1–7) and some selected C\*-series (C1–2) tests are presented here; principal stress rotation is imposed under increasing or constant  $q$ , in B- or C-series tests, respectively, and instability is triggered during the first half of the first stress rotation cycle in these tests. Specimens B1 (and B4), B2 (and B5) and B3 are consolidated at  $K_c = 0.80, 0.50$  and  $0.40$ , respectively, to mean effective stress  $p'_c = 200$  kPa, while specimens B6 and B7 are consolidated at  $K_c = 0.50$  and  $0.40$ , respectively, to  $p'_c = 100$  kPa. Specimens C1 and C2 are consolidated at  $K_c = 0.48$  and  $0.66$ , respectively, to  $p'_c = 200$  kPa. Consequently, the combined effects of consolidation and loading history on the undrained

behaviour of loose AC M31 Sand are investigated. Emphasis is placed on figuring out if flow instability is triggered under undrained principal stress rotation when the stress path crosses the initial IS.

Figure 6a shows the ESPs in the  $q_d - p'$  plane from tests B1–3 and C1–2. The labels attached to hollow circles indicate the value of  $\alpha$  at the respective stress states, while the solid circles and the corresponding labels refer to the IPs. The constant- $q_d/p'$  broken lines represent the ILs for different angles  $\alpha$ , determined in A-series tests. It should be noted that the PTP in test C2 was not recorded due to low-frequency data acquisition ( $f = 0.5$  Hz). To avoid false interpretation of the test results due to plotting sparsely recorded data points, the location of the PTP is estimated in test C2, based on the data collected with confidence from tests A17 ( $K_c = 1.00$ ) and C6 ( $K_c = 0.64$ ) in which phase transformation occurred at  $\alpha_{\sigma'1} = 86.2^\circ$  and  $76.2^\circ$ , respectively, and the unloading branch of the ESP C2 is assumed to be described by the broken line that follows the ESP A17. Figure 6b shows the rotational capacity at different levels of shear strain and at the IP exhibited in tests B1–5 and C1–2.

Figure 6a and b shows that in B-series tests a particular level of shear strain  $\gamma_{oct}$  and instability are induced by a lower increase in  $\Delta\alpha_{\sigma'1}$  and  $q_d$  when  $K_c$  is lower;  $\Delta\alpha_{\sigma'1}$  expresses the monotonic increase in  $\alpha_{\sigma'1}$ . This result indicates the high flow potential and vulnerability of sand to small undrained perturbations of  $\alpha_{\sigma'1}$  and  $q_d$  when the static shear stress is high [22, 67]. However, sand consolidated at higher  $K_c$  suffers in a different way: lower peak- $q_d$  and

minimum- $q_d$  strengths are mobilised due to a higher value of  $\alpha$  at the IP and PTP, respectively, and due to a lesser expansion of the LBS during anisotropic consolidation [65, 67, 85]. It can be also seen that the rotational capacity  $\Delta\alpha_{\sigma'1}$  at a particular  $\gamma_{oct}$  and at the IP under constant- $q$  loading is higher than that under increasing  $q$  loading for a given value of  $K_c$ ; for example, one may compare the ESPs B2 and C1. The importance of the position of the ESP in relation to the LBS is highlighted here. It is noted that the ESPs from B-series tests correspond to traces along different LBSs depending on the value of  $K_c$ .

Figure 7 shows selected ESPs in the deviatoric plane from A-, B- and C\*-series tests. The IPs are marked with solid (or hollow) circles and squares in the case of IC and AC sand, respectively. It appears that flow instability is triggered under undrained principal stress rotation when the stress path crosses the initial IS. These results indicate that the mobilised  $\varphi$  at a given  $\alpha$  when flow is triggered does not depend on the consolidation stress ratio,  $K_c = \sigma'_3/\sigma'_1$ , or the stress history that precedes the mobilisation of the state  $(\alpha, \varphi)_{ip}$ , verifying the findings of [49, 67]. However, it should be noted that the angle between the ESP and the IS at the intersection point is large in all cases shown in Fig. 7.

Some of the ESPs shown in Fig. 7 exhibit an interesting feature post-peak indicating that stress rotation occurs towards  $\alpha_{\sigma'1} = 0^\circ$  or  $90^\circ$  during the unstable flow because the stress  $Y_s$  is unloaded non-proportionally to the stress  $X_s$ . This spontaneous behaviour, which is also observed in radial loading tests, is a typical example of bifurcation

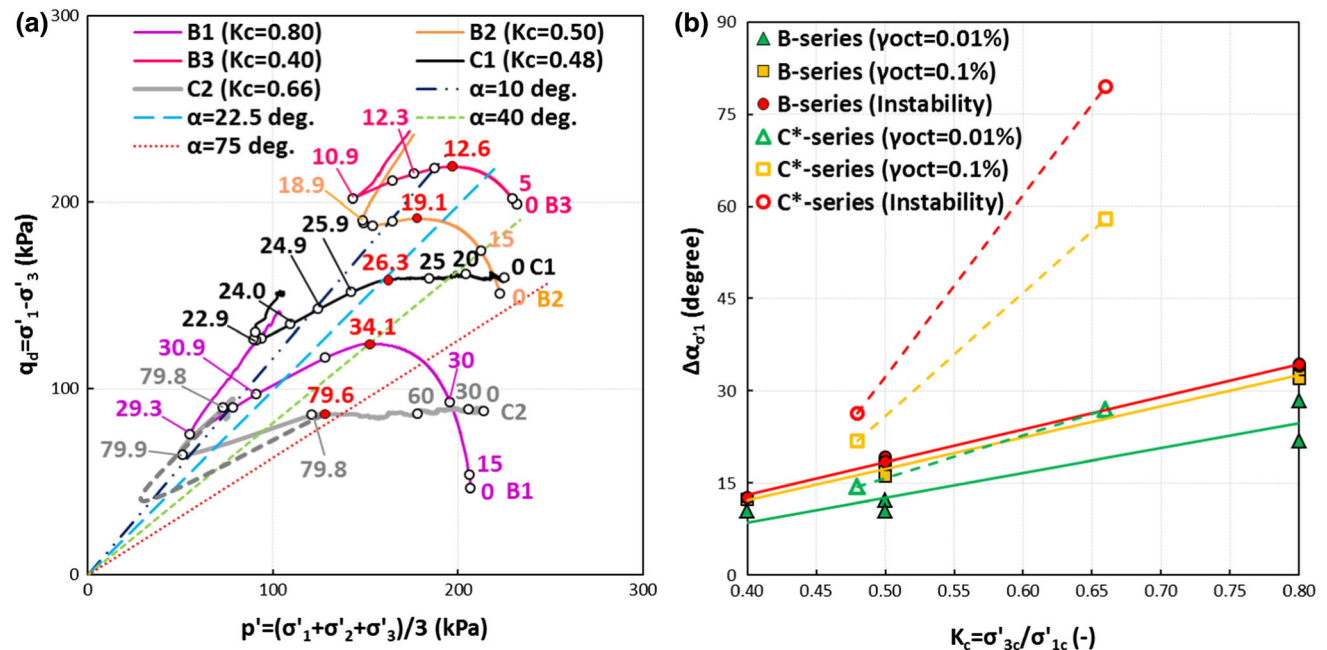
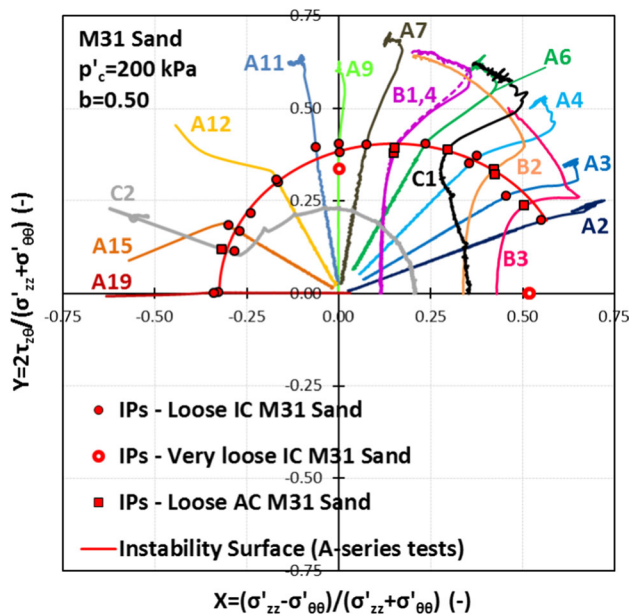


Fig. 6 Response of loose anisotropically consolidated sand to monotonic undrained loading with rotating stress principal axes. a Stress paths in the  $q_d - p'$  plane. b Rotational capacity,  $\Delta\alpha_{\sigma'1}$ , at various levels of shear strain and at the instability point against  $K_c$



**Fig. 7** Stress paths and instability points from A-, B- and C\*-series tests in the deviatoric plane

since unpredictable, non-unique routes are followed in the stress space depending on the imperfections and perturbations in the system (specimen–apparatus). However, some bifurcated ESPs progress in chorus, irrespective of the type of loading history (e.g. B1, A6, C1, A4), and in a repetitive pattern (e.g. B1, B4). This behaviour is typically attributed to traversing a boundary surface [59, 68] and indicates that the recorded bifurcated response is still of physical relevance. Moreover, the phenomenon is more intense when instability is triggered in the zones  $22.5^\circ \leq \alpha_{\sigma'1} \leq 35^\circ$  and  $60^\circ \leq \alpha_{\sigma'1} \leq 75^\circ$ , that is when one of the planes of maximum stress obliquity aligns with the horizontal bedding plane or when strong non-coaxiality is exhibited with  $\alpha_{de1}$  close to  $45^\circ$ ; for example, the angle between the two characteristic planes is  $4^\circ$  at the IP in test A12, while the direction angles  $\alpha_{\sigma'1}$  and  $\alpha_{de1}$  are  $34.1^\circ$  and  $42.7^\circ$ , respectively, at the IP in test B1. It is, thus, queried whether the governing (and repeatable) imperfection is a material feature, such as the bedding plane, or a perturbation in the system related to the apparatus, boundary conditions and stress–strain non-uniformities. A discussion on this subject is presented in Sect. 5.

### 4.3 Undrained behaviour of loose AC sand under monotonic loading with rotating stress principal axes: triggering of flow beyond the initial instability surface

In this section, it is shown that the previously established IS can be crossed stably when loose AC M31 Sand is subjected to undrained rotation of the stress PA under constant

deviatoric stress. Instability is actually triggered when the LBS is probed in the post-peak regime with an outwards direction. Figure 8a and b shows the ESPs from tests C3 to C6 in both stress spaces; the symbolisms in Fig. 8a are the same as those in Fig. 6a. The tested specimens have a void ratio between 0.704 and 0.721 and are consolidated at  $K_c$  between 0.64 and 0.75 (Table 2). It can be seen that under these combinations, which correspond to static stress difference,  $q_d$ , higher than the minimum strength exhibited in A-series tests at  $\alpha_{\sigma'1} \geq 45^\circ$ , at least one full stress rotation cycle is performed before the triggering of instability. It is noted that  $\alpha_{\sigma'1}$  changes from  $0^\circ$  to  $90^\circ$  and then from  $-90^\circ$  to  $0^\circ$  during a full stress rotation cycle ( $\Delta\alpha_{\sigma'1} = 180^\circ$ ), in accordance with the convention used herein.

The labels attached to hollow circles in Fig. 8a indicate the value of  $\alpha_{\sigma'1}$  at the respective stress states, while the solid rhombuses indicate the IPs and the corresponding labels indicate the value of  $\alpha_{ip}$ . In the case of ESP C6, the solid rhombus is the state at which the material fails at peak  $q_d/p'$  and the controllability of the loading programme is lost [52], while flow instability is triggered at another failure state marked with a square symbol that has an x at its centre; the sand, actually, flows after stress rotation is imposed on the failure surface. Curve fitting to the red rhombuses in the  $Y$ – $X$  plane (Fig. 8b) yields the so-called evolved instability surface (dashed line) which is a part of an ellipse (with its major axis coinciding with the  $X$ -axis and its minor axis being parallel to the  $Y$ -axis at  $X > 0$ ) located between the initial IS (solid line) and the failure surface. It is noted that the initial and evolved ISs are the loci of instability states observed in a set of loading tests with similar characteristics. There are, actually, an infinite number of such surfaces, with no intrinsic value, that can be revealed by different stress–strain histories [15]. Nevertheless, the utility of these conceptual artefacts is to highlight that the triggering condition of flow depends on the stress–strain history, while the pattern of flow depends on how close to the failure surface the instability is triggered.

The stress history effects on the flow triggering condition are highlighted in Fig. 9 that shows the initial IS, the evolved IS, the failure surface and the stress path C6 in the  $\varphi$ – $\alpha_{\sigma'1}$  plane. The solid circles and squares indicate the IPs from A-, B- and C\*-series tests (C1–2). These IPs are essentially located on the initial IS, while the two hollow circles correspond to very loose sand (specimens A1 and A10) and are located on a different initial IS. The solid rhombuses indicate the IPs from C-series tests (C3–C6) during which the instability is triggered past the first stress rotation cycle; these IPs are located on the evolved IS. The x-square indicates the post-failure IP in test C6. Figure 9 shows that flow is triggered at different  $\varphi_{ip}$ , namely  $20.0^\circ$ ,  $25.6^\circ$  and  $39.1^\circ$ , for a given  $\alpha_{\sigma'1}$  of around  $60^\circ$ , each of



small when shearing is imposed along the bedding plane [41]. The minimum  $\varphi$  is exhibited in the range of  $\alpha_{\sigma'1}$  between  $60^\circ$  and  $75^\circ$ , indicating that some characteristics of the initial fabric, e.g. the horizontal bedding plane, may endure even when sand is sheared to peak failure. Jiang et al. [34] reported similar peak failure characteristics under homogeneous conditions for a granular material with inclined bedding plane tested, in conventional triaxial compression mode under rigid boundary conditions, using the discrete element method (DEM), while Chen and Huang [8] incorporated this type of non-monotonic variation of peak stress ratio with  $\alpha_{\sigma'1}$  in their model.

The strain history effects on the triggering condition and deformation pattern of flow are highlighted in Fig. 10. The normalised excess pore-water pressure,  $\Delta u/p'_i$ , at the IP and PTP is plotted against  $\alpha_{\sigma'1}$  for the A- and C-series (C3 to C6) tests; in this figure, it is considered that  $\alpha_{pt} \equiv \alpha_{ip}$  and the value of  $\Delta u/p'_i$  at the (not recorded) PTP in test C5 is estimated, as in the case of test C2. In order to distinguish the plastic contraction occurring unstably during flow from that occurring stably before the triggering of flow [6] and quantify indirectly the former, the flow parameter  $U_1 = (u_{pt} - u_{ip})/p'_i$  is introduced. DEM simulations have shown that the stress unloading (i.e. the decrease in  $q_d$  and  $p'$ ) occurring during the isochoric flow of granular materials is related to a loss of grain-to-grain contacts and weakening of the force-bearing grain structures [25, 27]. The parameter  $U_1$  may express macroscopically this type of

destruction, which is stress–strain history dependent, as shown next.

Figure 10 shows that in A-series tests the ratio  $(\Delta u/p'_i)_{ip}$  is practically constant at 0.30, irrespective of  $\alpha_{\sigma'1}$ , while the ratio  $(\Delta u/p'_i)_{pt}$  is equal to 0.44 at  $\alpha_{\sigma'1} = 10^\circ$ , increases to the maximum level of 0.90–0.91 in the range of  $\alpha_{\sigma'1} = 60^\circ$ – $75^\circ$  and then decreases mildly to 0.83, at  $\alpha_{\sigma'1} = 90^\circ$ . On the other hand, in C-series tests (C3 to C6) the ratio  $(\Delta u/p'_i)_{ip}$  is 0.68–0.69 when  $\alpha_{\sigma'1}$  ranges between  $57.4^\circ$  and  $64.4^\circ$  and decreases to 0.55 when  $\alpha_{\sigma'1}$  ranges between  $79.6^\circ$  and  $90.0^\circ$ , while the ratio  $(\Delta u/p'_i)_{pt}$  is around 0.85 when  $\alpha_{\sigma'1}$  ranges between  $57.4^\circ$  and  $90.0^\circ$ . An important conclusion is that the ratio  $(\Delta u/p'_i)_{pt}$  is practically unaffected by the type of stress history (when  $K_c \geq 0.64$ ) and depends only on  $\alpha_{pt}$ , while the ratio  $U_1 = (u_{pt} - u_{ip})/p'_i$  is drastically reduced in stress rotation tests C3 to C6. Similar findings concerning the dependence of  $(\Delta u/p'_i)_{pt}$  on  $\alpha_{pt}$ , which is likely the result of inherent anisotropy, are reported by Yoshimine et al. [83, 84]. It is noted that a lower value of  $U_1$  corresponds to a higher value of  $\sin \varphi_{ip}$  (in C-series tests), indicating that the pattern of flow becomes less contractive at a given  $\alpha_{\sigma'1}$  when the triggering occurs nearer to the failure surface, possibly due to the induced-anisotropy effects.

Figure 11a, b shows the ESP from test C3 in both stress spaces. The ESPs from tests A8 and A13, conducted on specimens with  $e$  similar to that of specimen C3, are also shown in Fig. 11a, in order to visualise the LBS of IC sand at  $\alpha_{\sigma'1} = 45^\circ$  and  $60^\circ$ . In this study, the LBS of sand consolidated at  $\alpha_{\sigma'1} = 0^\circ$  and  $K_c \geq 0.60$  is found to coincide in the post-peak regime with that of IC sand when  $\alpha_{\sigma'1} \geq 45^\circ$ ; similar behaviour is reported in [65]. The ESP C3 probes the initial IS at  $\alpha_{\sigma'1} = 45^\circ$ , with  $\varphi = 22.1^\circ$ , during the fifth stress rotation cycle (point 1), yet stability is sustained until the LBS is probed at  $\alpha_{\sigma'1} = 57.4^\circ$ , with  $\varphi = 25.6^\circ$  (point 2), in the same cycle. It is noted that the initial IS is probed at a small angle (almost tangentially), while the LBS is probed outwards. Moreover, the less steep of the maximum stress obliquity planes makes an angle of  $11^\circ$  with the bedding plane at point 1, while it coincides with it at point 2. These results indicate that the IP under undrained principal stress rotation is attracted to stress combinations  $(\alpha_{\sigma'1}, \varphi)$  that correspond to unfavourable deformation kinematics.

The pairs of points 3–4 and 5–6 in Fig. 11b represent the initiation and termination of two strong strain localisation events at large strains (nominal  $\gamma_{oct} \approx 16\%$  and  $18\%$ , respectively), captured by means of visual inspection and interpretation of stresses and strains; weak strain localisation, with undetectable effects on the global measurements, is firstly observed at point H ( $\gamma_{oct} = 8.2\%$ ) when strength is regained past the PTP in dilative mode. The nominal values of  $\alpha_{\sigma'1}$  and  $\varphi$  indicate that the less steep of the maximum

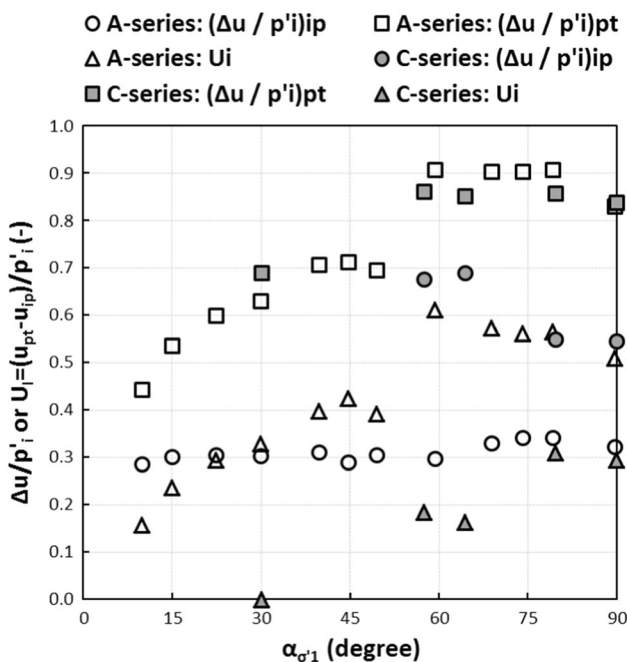
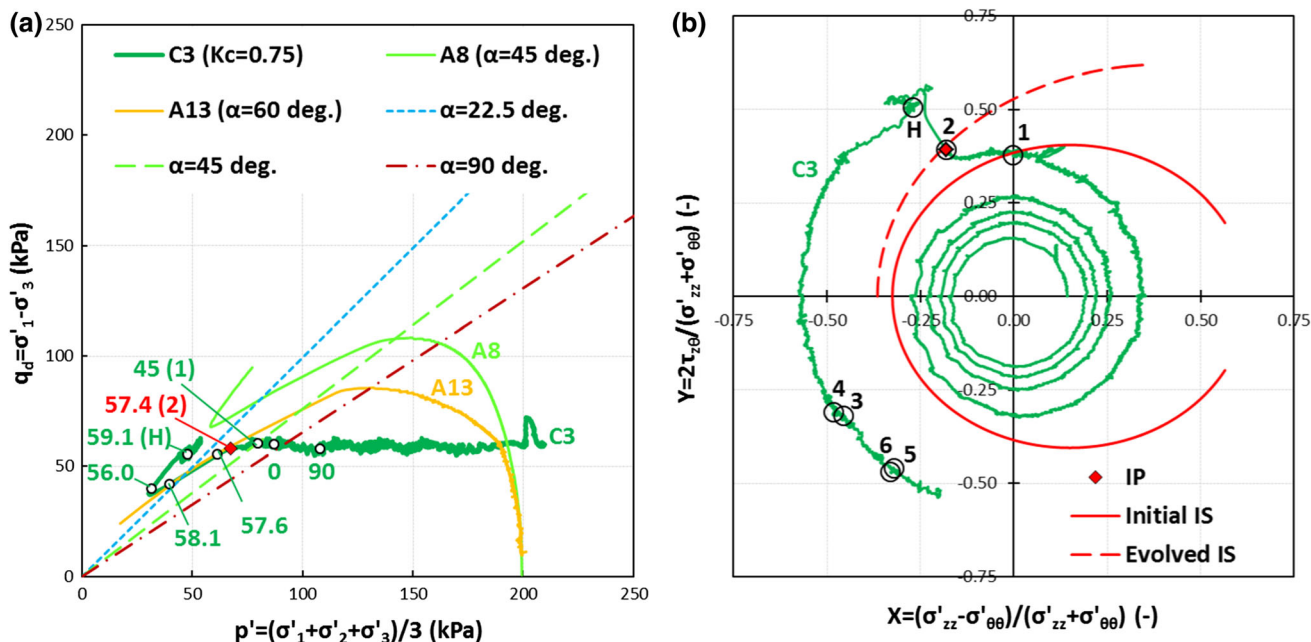


Fig. 10 Strain history effects on the triggering condition and deformation pattern of flow of loose sand: normalised excess pore-water pressure,  $\Delta u/p'_i$ , and flow parameter,  $U_1$ , against the principal stress direction angle,  $\alpha_{\sigma'1}$ , at the instability and phase transformation point



**Fig. 11** Response of loose anisotropically consolidated sand to monotonic undrained loading with rotating stress principal axes. **a** Stress path from test C3 in the  $q_d - p'$  plane. **b** Stress path from test C3 in the  $Y-X$  plane

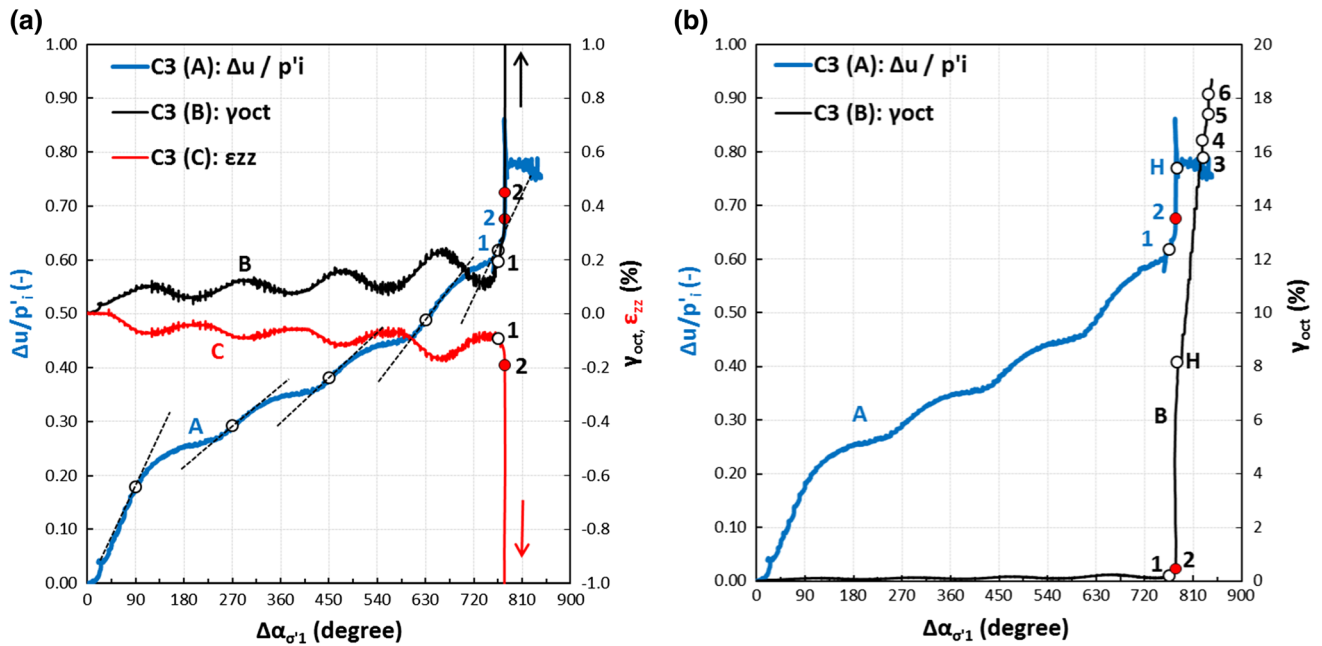
stress obliquity planes makes an angle of  $11^\circ$  with the bedding plane at points 3 and 4, while it coincides with it at points 5 and 6. Thus, the localised bifurcations under undrained principal stress rotation may, also, be triggered preferably at stress states corresponding to unfavourable deformation kinematics. However, the loss of deformation homogeneity inhibits an interpretation with confidence. It is noted that the diffuse bifurcation is triggered before the localised in the course of monotonic loading [17, 46, 51].

Figure 12a, b shows the evolution of the normalised excess pore-water pressure,  $\Delta u/p'_i$ , shear strain,  $\gamma_{oct}$ , and normal strain,  $\epsilon_{zz}$ , with  $\Delta\alpha_{\sigma'_1}$  in test C3. The hollow circles without label indicate, here, the states with  $\alpha_{\sigma'_1} = 90^\circ$ , while the points 1 to 6 and H are the same as before. The slope  $d(\Delta u/p'_i)/d\Delta\alpha_{\sigma'_1}$  at  $\alpha_{\sigma'_1} = 45^\circ$  during the fifth stress rotation cycle (point 1) is similar to that at  $\alpha_{\sigma'_1} = 90^\circ$  during the first cycle, being steeper compared with that at  $\alpha_{\sigma'_1} = 90^\circ$  during the intermediate cycles; the local tangents are displayed to highlight this interesting strain history memory effect that is possibly related to the inherent anisotropy of sand and acts as a precursor for instability [47]. It is worth noting that memory parameters are frequently incorporated into bounding surface plasticity models [12, 13, 42, 56] and determine the value of the so-called plastic modulus, the evolution of which can be monitored in order to predict the triggering of instabilities [46]. Furthermore, the effect of the induced anisotropy is also apparent in the evolution of strains since the local maximum of  $\epsilon_{zz}$  and  $\gamma_{oct}$  in each stress rotation cycle (under

stable conditions) occurs well beyond the state with  $\alpha_{\sigma'_1} = 90^\circ$  [72].

The values of  $(\Delta u/p'_i)_{pt}$  and  $U_I$  are 0.86 and 0.18, respectively, in test C3. If the comparison is made with the respective values in test A11, which are 0.70 and 0.39, it can be inferred that the looser specimen C3 ( $e = 0.721$ ), which flowed along the stress direction  $\alpha_{ip} = 57.4^\circ$ , is less contractive during flow than the denser specimen A11 ( $e = 0.699$ ), which flowed at  $\alpha_{ip} = 49.5^\circ$ . This is also validated by the values of accumulated  $\gamma_{oct}$  at the PTP, which are 3.93% and 3.54%, respectively. Apparently, the stress-strain history that precedes the triggering of flow influences the subsequent flow deformation pattern albeit the ratio  $(\Delta u/p'_i)_{pt}$  depends only on  $\alpha_{pt}$  and  $e$  (see Fig. 10).

The post-flow dilatancy behaviour of the specimen C3 is investigated next. The ratio  $\Delta u/p'_i$  decreases from 0.86, at the PTP, to 0.77, at point H, as  $\gamma_{oct}$  increases from 3.9 to 8.2% (Fig. 12). Thereafter, the stress PA is rotated from  $\alpha_{\sigma'_1} = 59.1^\circ$ , at point H, to  $\alpha_{\sigma'_1} = -72.5^\circ$ , at point 3, under practically constant  $\eta = q/p' = 1.00$  (or  $q_d/p' = 1.16$ ) and  $\Delta u/p'_i = 0.77$ , while  $\gamma_{oct}$  increases to 15.8% (Figs. 11 and 12). The sand deforms in an undrained steady state similar to that observed in the DEM simulations of drained principal stress rotation tests performed by [44, 71, 73], exhibiting no plastic volume change but not being in a critical state [45, 59, 62] since the void ratio is lower than the critical void ratio at the current mean effective stress,  $e < e_c(p')$ , and the stress direction changes. Two strong localisation events are triggered at points 3 and 5 (Fig. 13), and the pore-water pressure measured at the base of the



**Fig. 12** Evolution of the normalised excess pore-water pressure,  $\Delta u/p'_i$ , shear strain,  $\gamma_{oct}$ , and normal strain,  $\epsilon_{zz}$ , during undrained principal stress rotation in test C3 (the curves of  $\gamma_{oct}$  and  $\epsilon_{zz}$  are zoomed in **a**)

specimen decreases (Fig. 12) possibly because the sand inside the shear zones shows a tendency to dilate (or dilates to some degree) in order to attain a true critical state [16, 78].

Figure 13a–d shows the photographs of the specimen in test C3 at different levels of  $\gamma_{oct}$ , while Fig. 13e shows the strain path in the  $Y_\epsilon - X_\epsilon$  plane. The capturing of localised instabilities is achieved by analysing the photographic material and interpreting the evolution of stresses and strains. Figure 11b shows that the stress path in the  $Y - X$  plane moves backwards from point 3 to point 4, while Fig. 13e shows that the strain path in the  $Y_\epsilon - X_\epsilon$  plane becomes perturbed at points 3 and 5 as the specimen deformation is accelerated and turns suddenly into the simple-shear mode ( $\alpha_{d,e1} = -45^\circ$ ). The photograph in Fig. 13b is taken at point H, at shear strain  $\gamma_{oct} = 8.2\%$ . Some faint signs of strain localisation are observed since the grid lines on the membrane become wavy at some places and the specimen shows a slight neck at its lower part. Figure 13c shows the specimen at point 3, at nominal shear strain “ $\gamma_{oct}$ ” = 15.8%, just before the triggering of the first strong localisation event. The grid lines at point 3 are wavier compared to the grid lines at point H but show the same inclination angle along the height of the specimen, while a discernible neck is observed at the lower part of the specimen. The photograph in Fig. 13d, taken at the end of testing, shows that the upper part of the specimen has been deformed in an extensional mode, while the lower part has been deformed in an extensional–torsional mode, indicating that the simple-shear deformation was localised in the lower part.

Novel results are presented in Fig. 14 which shows the ESP C6 in both stress spaces moving from the consolidation state to the failure state in a stable mode while the effective stresses are isotropically unloaded; note that the initial IS is probed at different points either tangentially (point 2) or at a small angle. At point 3 ( $\gamma_{oct} = 1.7\%$ ) the material fails at peak  $q_d/p'$  (or  $\eta = qp'$ ) and the pore-water pressure begins to decrease, indicating that mild plastic dilation occurs under homogeneous deformation. Concurrently, the stress difference,  $q_d$ , begins to decrease, partly due to the membrane stretching and partly due to the material response, the controllability of the loading programme is lost and the sand softens as the stress state moves obligingly along the anisotropic failure surface (see Fig. 9 and [68]). The loss of controllability in a quasi-static mode indicates the triggering of a non-flow diffuse instability under increasing stresses ( $d\sigma'_1, d\sigma'_2, d\sigma'_3 \geq 0$ ) and decreasing stress ratio ( $d\eta < 0$ ), verifying for the first time the predictions of the numerical directional analyses by Darve [66]. Afterwards, the pore-water pressure begins again to increase and dynamic flow instability is triggered on the failure surface at point 4 with  $\alpha_{\sigma1} = 64.4^\circ$ ,  $\phi_{ip} = 39.1^\circ$  and  $\gamma_{oct} \approx 6.6\%$  (the exact value of  $\gamma_{oct}$  is unknown because the angle-measuring potentiometer has gone out of range just before point 4). The induced-anisotropy effects on the flow behaviour are indicated by the value of  $U_1 = 0.16$  at  $\alpha_{\sigma1} = 64.4^\circ$  (see Fig. 10), in accordance with expectations [44, 80, 82]. Flow is terminated at the PTP (point 5), and thus three zero-dilatancy points are observed in this test.

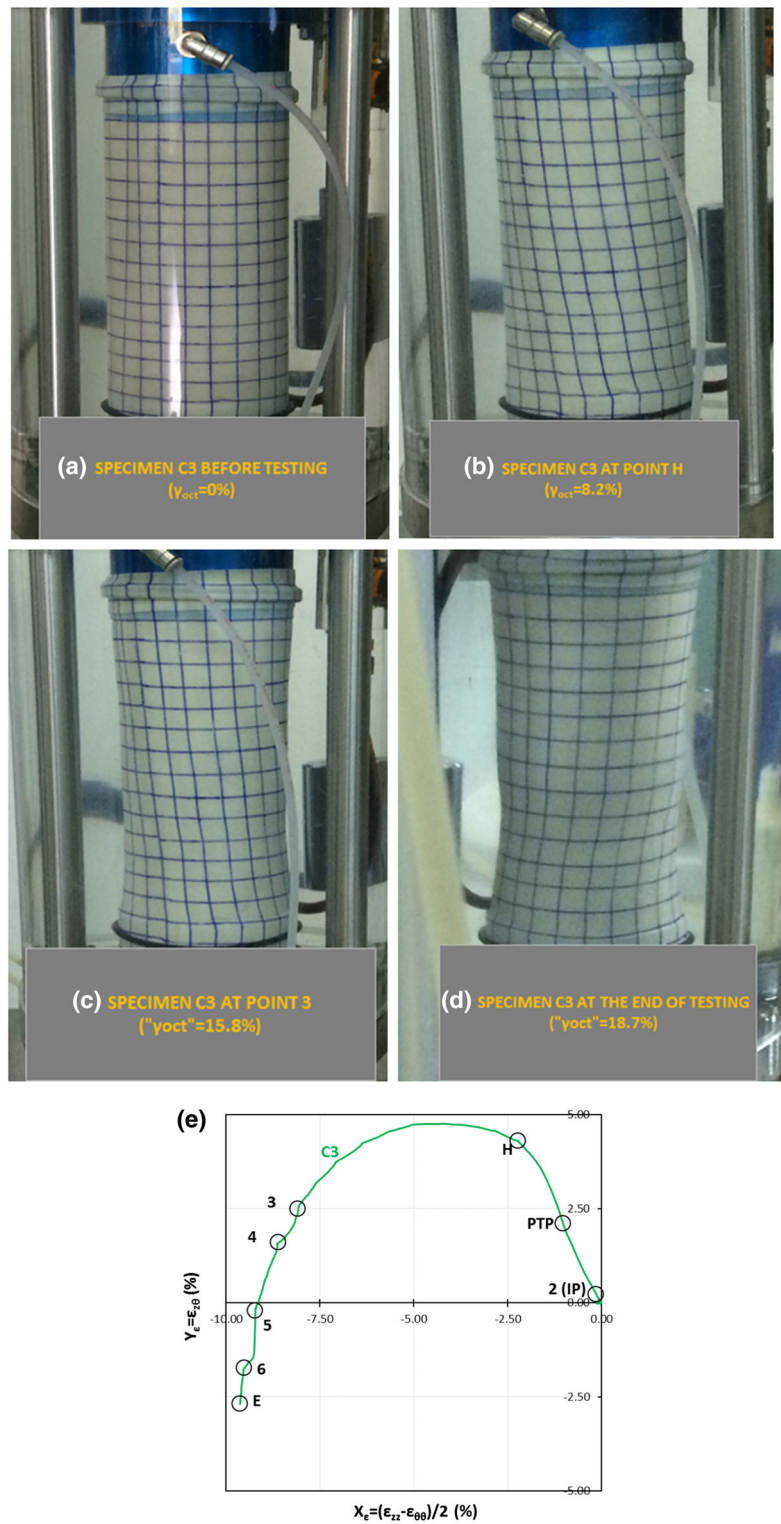


**Fig. 13** Photographs of the specimen (a–d) in test C3 at different levels of shear strain and strain path in the  $Y_{\epsilon}-X_{\epsilon}$  plane (e). **a** Specimen before testing ( $\gamma_{\text{oct}} = 0\%$ ). **b** Specimen at point H ( $\gamma_{\text{oct}} = 8.2\%$ ). **c** Specimen at point 3 ( $\gamma_{\text{oct}} = 15.8\%$ ). **d**. Specimen at the end of testing ( $\gamma_{\text{oct}} = 18.7\%$ ). The photographs were taken under the refraction induced by the crossing of light through the water–perspex–air interfaces (e on next page) **e** Strain path from test C3 in the  $Y_{\epsilon}-X_{\epsilon}$  plane



The type of perturbation that triggers flow in each of the tests C3 to C6 is discussed here. In test C3, the stress rotation induces, at  $\alpha_{ip} = 57.4^\circ$ , an increase in  $u$  and  $\eta$ , while it lowers the LBS and the corresponding minimum- $q_d$  strength; the incremental stress direction is parallel to the hydrostatic axis in the  $\sigma'_1-\sigma'_2-\sigma'_3$  space, while  $\alpha_{\sigma'_1}$  is increasing and  $b$  is kept constant. A similar destabilising perturbation is reported in [67]. In tests C4 and C5, a creep-induced increase in  $u$  and  $\eta$  (during the pause period between the steps of stress rotation) triggers flow, while the incremental stress direction is similar to that in test C3 but with different values of  $\alpha_{ip}$ . Similar results are presented in [38, 43]. In test C6, the ESP reaches the failure surface, while the value of  $q_d$  is lower than the minimum- $q_d$  strength corresponding to  $\alpha_{\sigma'_1} = 30.2^\circ$  (see Fig. 14a); hence, flow is not triggered [57, 68]. Flow is subsequently triggered under  $d\sigma'_1, d\sigma'_2, d\sigma'_3, d\eta < 0$  and  $du > 0$ , when stress rotation lowers the LBS (and minimum- $q_d$  strength) below the current  $q_d$ -level. From a microscopic point of view, the less steep of the maximum stress obliquity planes aligns with the bedding plane at that moment. This is a novel finding to the authors' best knowledge.

#### 4.4 Undrained behaviour of loose AC sand under loading with rotating stress principal axes and periodically changing deviatoric stress

It has been previously shown that stability is sustained when the initial IS is probed at small angles; this

incremental stress direction is followed spontaneously past the first stress rotation cycle, since the pore-water pressure develops freely under a decreased rate [32, 49, 81]. The stress rotation path D1, with the characteristics shown in Fig. 15, was designed to investigate further this behaviour. The monotonic stress rotation is performed continuously, and a very low frequency ( $f = 10^{-3}$  Hz) is applied to ensure homogeneous pore-water pressure inside the specimen.  $p$  is held essentially constant,  $b$  oscillates between 0.40, at  $\alpha = \pm 90^\circ$ , and 0.52, at  $\alpha = 0^\circ$ , and  $q$  changes in a periodic manner that ensures unloading in the extension regime, when  $\alpha_{\sigma'_1}$  changes from  $45^\circ$  to  $90^\circ$ . It is noted that the small change in  $b$  is not expected to alter significantly the LBS, especially in the extension regime [41, 64].

Figure 16 shows the ESP D1 in both stress spaces. It can be inferred that the partial control of the incremental stress direction, by means of deliberate unloading of  $q$ , postpones the triggering of flow. When the initial IS and LBS are probed almost concurrently in the vicinity of point 1, the incremental stress direction is tangential to the former and towards the interior of the latter and hence flow is not triggered. It is interesting to compare the ESPs D1 and C3 that probe the initial IS at approximately the same point in the  $Y-X$  plane. Flow of specimen D1 is only triggered at point 2, away from point 1, when the descending branch of the LBS is probed outwards. It is noted that the IPs in tests D1 and C3 are close in the  $\sigma'_1-\sigma'_2-\sigma'_3$  space and both ESPs follow the isotropic unloading direction, while the values of  $\alpha_{ip}$  are different. The comparison of the response of specimens D1 and A17 is also interesting: the values of

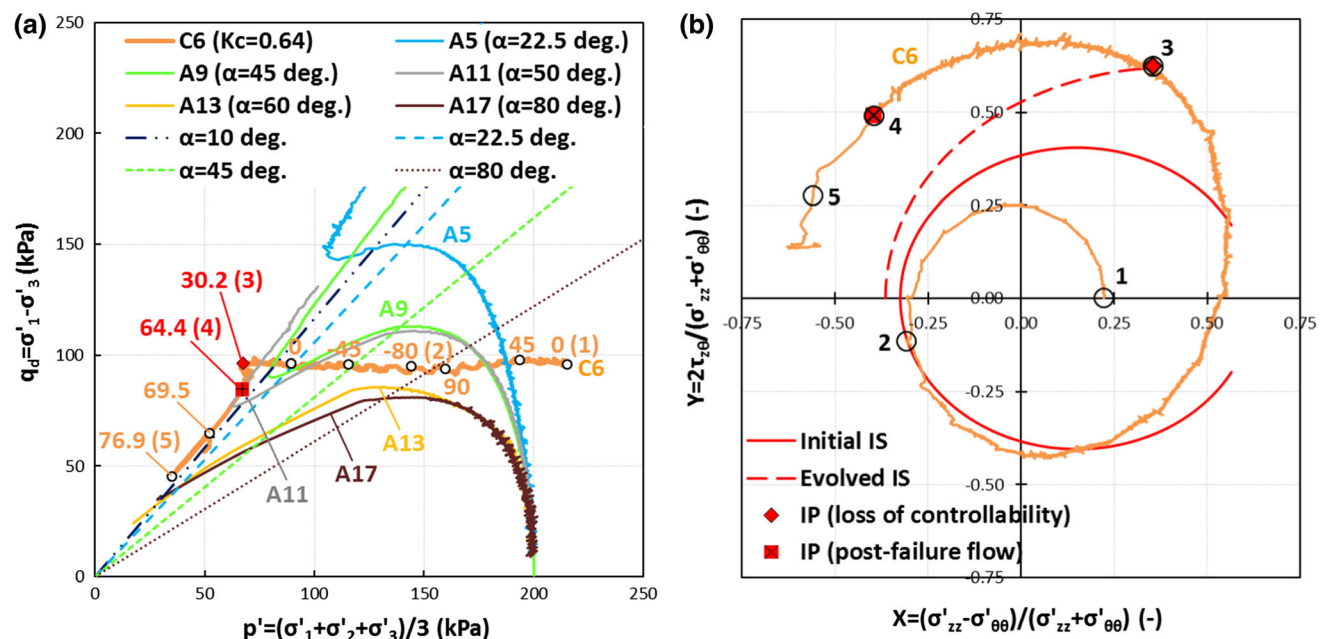


Fig. 14 Response of loose anisotropically consolidated sand to monotonic undrained loading with rotating stress principal axes. **a** Stress path from test C6 in the  $q_d - p'$  plane. **b** Stress path from test C6 in the  $Y-X$  plane

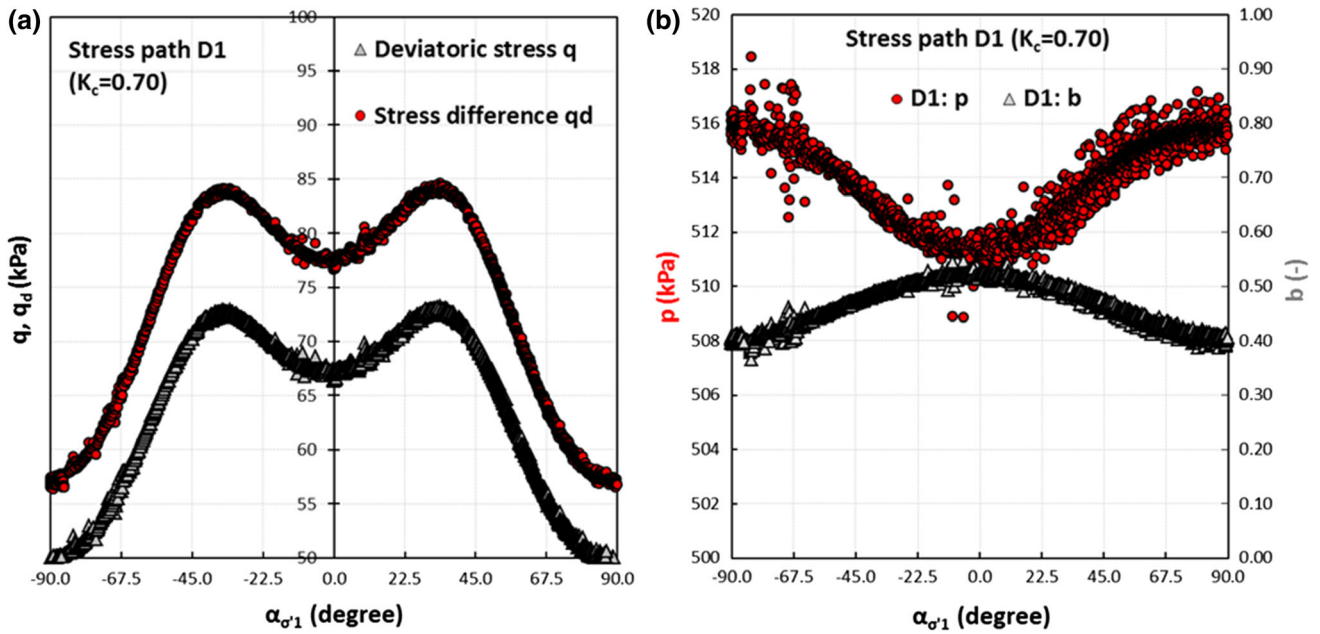


Fig. 15 Characteristics of stress path D1. **a** Periodic change of  $q$  and  $q_d$  with  $\alpha_{\sigma_1}$ . **b** Periodic change of  $p$  and  $b$  with  $\alpha_{\sigma_1}$

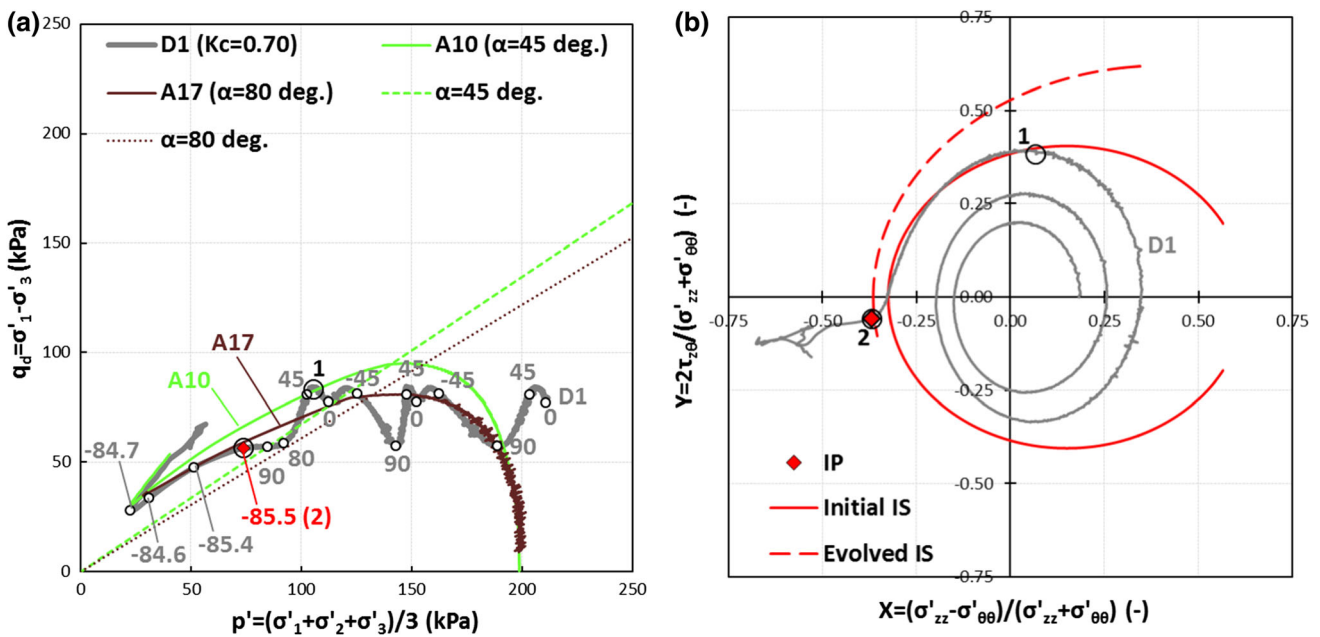
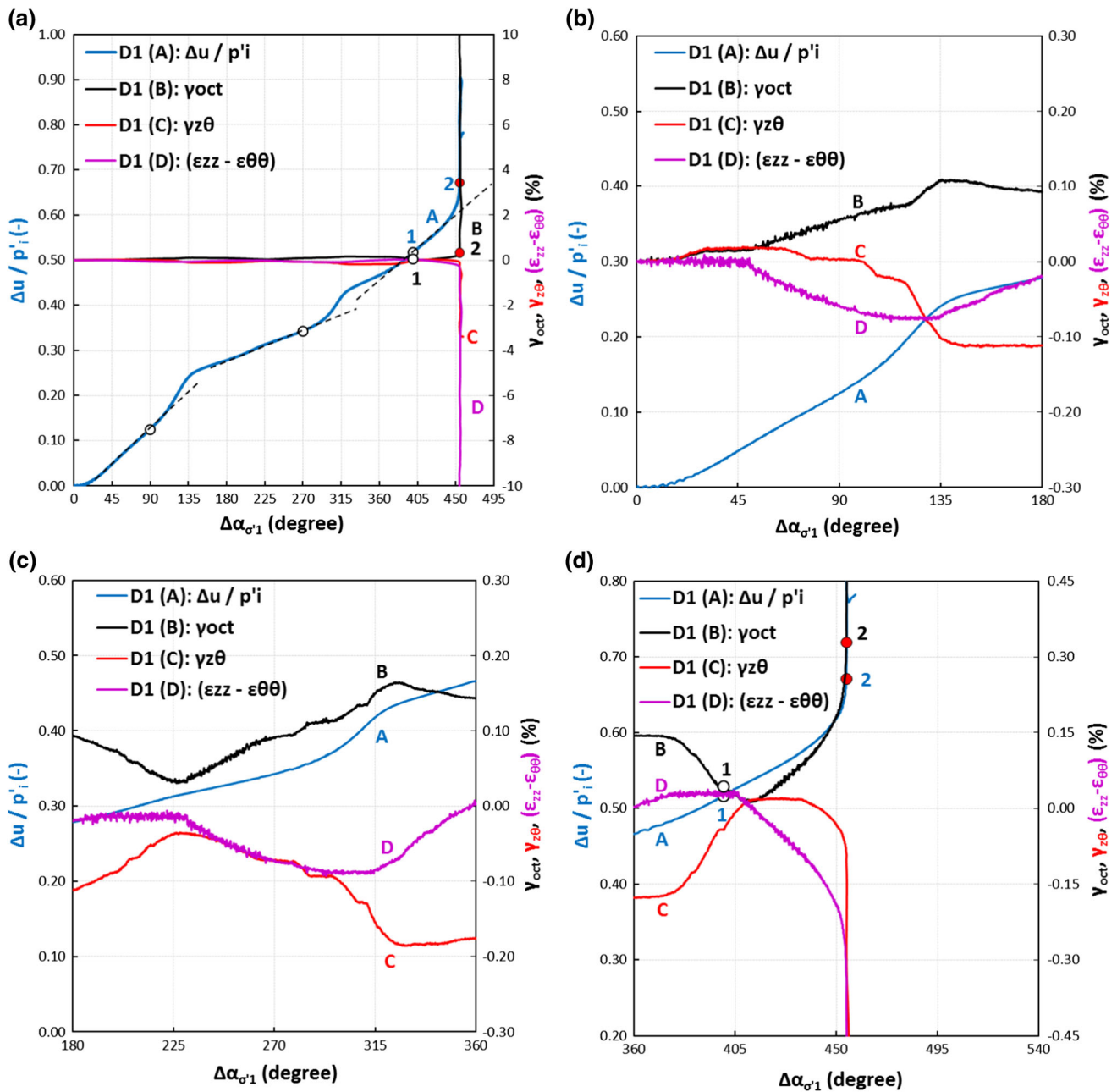


Fig. 16 Response of loose anisotropically consolidated sand to undrained loading with rotating stress principal axes and periodically changing deviatoric stress. **a** Stress path from test D1 in the  $q_d$ - $p'$  plane. **b** Stress path from test D1 in the  $Y$ - $X$  plane

$(\Delta u/p'_i)_{pt}$ ,  $U_I$  and  $\gamma_{oct,pt}$  are 0.90, 0.23 and 3.26%, and 0.91, 0.59 and 4.53%, respectively, indicating that the specimen D1, with  $e = 0.738$  and  $\alpha_{ip} = -85.5^\circ$ , is less contractive than specimen A17, with  $e = 0.727$  and  $\alpha_{ip} = 79.1^\circ$ , after the triggering of flow due to the stress-strain history effects.

Figure 17 shows the evolution of strains  $\gamma_{oct}$ ,  $\gamma_{z\theta}$  and  $(\varepsilon_{zz} - \varepsilon_{\theta\theta})$  and ratio  $\Delta u/p'_i$  with  $\Delta\alpha_{\sigma_1}$  in test D1. An

interesting observation is that the rotational rate  $d(\Delta u/p'_i)/d\alpha_{\sigma_1}$  at point 1 ( $\alpha = 40.0^\circ$ ), when the initial IS is probed during the third stress rotation cycle, has a similar value with the one at  $\alpha = 90^\circ$  during the first stress rotation cycle. This rate is rather related to the inherent anisotropy of sand, while the maximum rate developed stably is related to the increase in  $q$  (see Fig. 15a). One can notice in Fig. 17d that the strain increment  $d(\varepsilon_{zz} - \varepsilon_{\theta\theta})$  at point 1 is inert



**Fig. 17** Evolution of the normalised excess pore-water pressure,  $\Delta u/p'_i$ , and shear strains,  $\gamma_{oct}$ ,  $\gamma_{z\theta}$  and  $(\varepsilon_{zz} - \varepsilon_{\theta\theta})$ , during undrained principal stress rotation in test D1. **a** Complete stress rotation history. **b** First cycle of stress rotation. **c** Second cycle of stress rotation. **d** Third cycle of stress rotation

(irrespective of the assumption used for calculating  $\varepsilon_{\theta\theta}$ ) and only the mode  $d\gamma_{z\theta}$  contributes to the deformation. This means that  $\alpha_{d\varepsilon 1} = 45^\circ$  while the sand deforms homogeneously in simple shear, with the maximum shear distortion  $d\gamma$  occurring to  $z\theta$ -angles; the simple-shear deformation lasts from  $\alpha_{\sigma'1} = 20^\circ$  to  $45^\circ$ ; thus, the response turns from remarkably non-coaxial to unexpectedly coaxial. Miura et al. [48] suggested that this “simple-shear deformation mode must be due to the predominant sliding on bedding

plane” and observed that the shear deformability during drained stress rotation is maximum under these conditions.

## 5 Discussion on the bifurcated behaviour

A variety of bifurcated behaviours has been captured in this study: the response of the specimen–apparatus system becomes dynamic with a burst of kinetic energy when flow instability is triggered, while the stress path in the  $Y$ –

$X$  plane follows unpredictable routes associated with a predominant unloading of the  $Y_s$  stress when shearing and/or sliding occurs along the bedding plane; the mechanical states beyond Lade's IL become unsustainable without varying the control parameters; the triggering of both diffuse and localised instabilities occurs preferably at stress states corresponding to unfavourable deformation kinematics, as if the bedding plane acts as an imperfection, and sudden transitions to strong simple-shear deformation occur in both bifurcation modes. On the other hand, the observed behaviour of the system may be attributed to the stress–strain non-uniformities, deformation inhomogeneities and inertial phenomena due to the boundary conditions imposed on hollow-cylinder testing, as discussed next.

The bifurcated behaviour of the system in radial test A4 ( $\alpha_{\sigma_1} = 22.5^\circ$  and  $b = 0.50$ ) is investigated next. The boundary loads  $p_o$ ,  $p_i$ ,  $F$  and  $T$  (Fig. 1a) are controlled in this test under isochoric saturated conditions to yield:

$$d\tau_{z\theta} = c \quad (c \text{ is a positive constant}) \quad (1a)$$

$$d\sigma_{zz} = c \quad (1b)$$

$$d\sigma_{\theta\theta} = -c \quad (1c)$$

$$d\sigma_{rr} = 0 \quad (1d)$$

$$d\varepsilon_{zz} + d\varepsilon_{\theta\theta} + d\varepsilon_{rr} = 0 \quad (1e)$$

The total normal stresses, shear stresses and normal strains (elastoplastic) appearing in Eq. 1 are given in Table 1 and shown in Fig. 1; it is noted that the effective normal stresses are uncontrollable.

Owing to the lack of coaxiality of the principal axes of stress and plastic strain rate, the second-order work,  $d^2W$ , is given by the following relationship:

$$d^2W = d\sigma_{ij}d\varepsilon_{ij} = (d\sigma_{zz} - d\sigma_{\theta\theta})(d\varepsilon_{zz} - d\varepsilon_{\theta\theta})/2 + 2d\tau_{z\theta}d\varepsilon_{z\theta} \quad (2a)$$

or in a normalised form:

$$\begin{aligned} d^2W_{\text{norm}} &= d^2W / (||d\sigma|| ||d\varepsilon||) \\ &= d^2W / \left( \sqrt{(d(\sigma_{zz} - \sigma_{\theta\theta}))^2 + (2d\tau_{z\theta})^2} \right. \\ &\quad \left. \sqrt{(d(\varepsilon_{zz} - \varepsilon_{\theta\theta})/2)^2 + (d\varepsilon_{z\theta})^2} \right) \end{aligned} \quad (2.b)$$

with the repeated indices  $i, j = z, r, \theta$  summed over and taking into account that  $\varepsilon_{\text{vol}} = 0$  and  $b = 0.5$ . Consequently, the control parameters  $X_s = (\sigma_{zz} - \sigma_{\theta\theta})$  and  $Y_s = 2\tau_{z\theta}$  form energy–conjugate pairs [52] with the response parameters  $X_e = (\varepsilon_{zz} - \varepsilon_{\theta\theta})/2$ ,  $Y_e = \varepsilon_{z\theta}$ , respectively. Equation 1 corresponds to the loading programme A4, while Eq. 2 is valid for any isochoric loading programme with  $b = 0.5$  performed herein.

Figure 18a shows the evolution of the normal stresses  $\sigma'_1, \sigma'_2, \sigma'_3$  (left vertical axis) and shear stresses  $Y_s/2$  and  $X_s/2$  (right vertical axis) with  $p'$  in test A4, while Fig. 18b shows the evolution of  $d^2W_{\text{norm}}$  (left vertical axis) and  $Y_s/2$  and  $X_s/2$  (right vertical axis) with  $p'$  up to the PTP in test A4. The hollow and solid circles represent the transient-peak and instability state, respectively, with the latter mobilised just after the former during monotonic loading; this behaviour is the result of increasing area of specimen's cross section, membrane stretching and requirement for accelerated strain development at the IP. The vertical dashed lines in Fig. 18a divide the peak-to-phase transformation response into three phases of one second each; it is noted that the pre-peak response lasted for 456 s. At the IP, the stresses  $Y_s$  and  $X_s$  begin to decrease, the development of strains is accelerated and the sign of  $d^2W_{\text{norm}}$  changes from positive to negative, indicating the loss of strength, stability and controllability which are later recovered at the PTP when  $d^2W_{\text{norm}}$  becomes positive again. The bifurcation of the shear stress paths is easily conceived since the unloading of  $Y_s$  is predominant when control is lost. The question is now straightforward: Which is the governing imperfection in the system that induces the observed bifurcated pattern?

*Inertial response of the loading system:* Since the deformation is accelerated post-peak, it may be suggested that the observed behaviour is due to the inertial specimen–apparatus interaction. However, the measurement of the boundary vertical displacement showed that, during the first and third phase of the peak-to-phase transformation response, the velocity is practically constant ( $\sim 10^{-2}$  mm/s and  $10^0$  mm/s, respectively), while during the second phase, the acceleration is practically constant and of the order of  $10^{-4}$  g ( $g = 9.81$  m/s<sup>2</sup>); similarly, the angular acceleration divided by the average radius of the annular specimen is of the order of  $10^{-4}$  g. Moreover, the vertical-displacement and torsional-angle change from peak to phase transformation is only 1.8 mm and  $7.4^\circ$ , respectively; hence, the pneumatic actuators function without problems, while no dynamic pressure changes are observed in the cell environment. Apparently, the bifurcated response is not due to inertial effects.

*Stress–strain non-uniformities:* It is well known that the stresses and strains across the wall of the hollow-cylinder specimen are not uniform, as a result of the torque-induced shear stress and strain on the curved wall, and of the pressure difference  $p_i - p_o$ ; non-smooth rigid ends induce further non-uniformities [29, 61]. Generally, the non-uniformities increase with  $\sin\varphi$  and with  $p_i - p_o$  or  $p_i/p_o$ . Ultimate limits to the values of  $p_i/p_o$  are physically imposed (via implosion/explosion of the specimen), while more strict limits ensure acceptable non-uniformities for

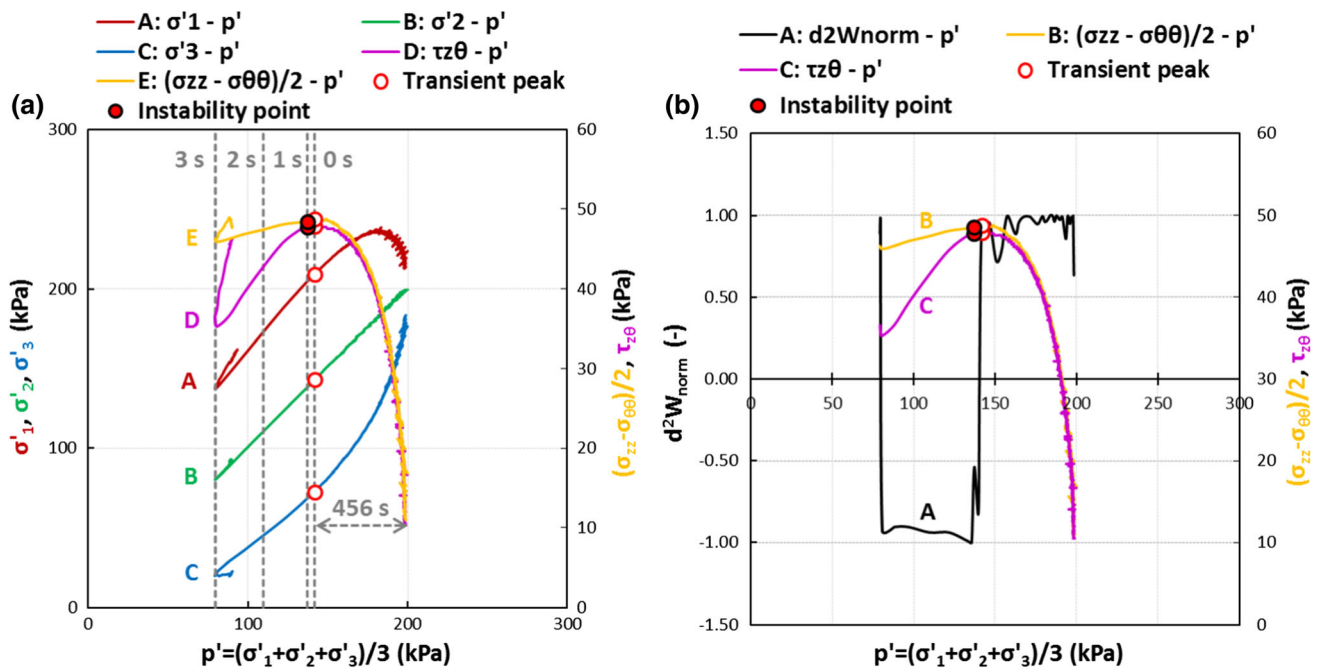


**Fig. 18** Bifurcation and instability in test A4. **a** Evolution of normal and shear stresses with  $p'$ . **b** Evolution of normalised second-order work and shear stresses with  $p'$

different specimen geometries and different stress paths. For example, Nakata et al. [49] applied the limits  $0.75 < p_i/p_o < 1.30$  for specimen dimensions  $H/D_o/D_i = 200/100/60$  (in mm) and for radial testing at  $b = 0.5$ . Figure 19 shows the evolution of  $p_i/p_o$  with  $\gamma_{oct}$  in A-series tests performed herein with  $H/D_o/D_i = 140/70/40$  (in mm). It can be seen that the ratio  $p_i/p_o$  varies within the permissible limits for  $\gamma_{oct}$  up to 8%. Testing at  $\alpha_{\sigma'_1} = 0^\circ$  and  $b = 0.5$  suffers from high values of  $p_i/p_o$  at low strains and excessive specimen bulging at high strains; hence, the interpretation of the response past the IP is avoided. The values of  $\gamma_{oct}$ ,  $\gamma_{z\theta}$ ,  $p_i/p_o$  and  $\varphi$  at the IP in test A4 are 0.50%, 0.49%, 1.06 and  $29.9^\circ$ , respectively, while the angles  $\alpha_{\sigma'_1}$  and  $\alpha_{d_{el}}$  are  $22.3^\circ$  and  $31.1^\circ$ , respectively. These results indicate that the bifurcation observed in Fig. 18 is rather related to the inherent anisotropy of sand and not to the stress–strain non-uniformities at the IP.

**Strain localisation:** Strain localisation is the major factor that impedes the investigation of the true soil behaviour in laboratory testing [17]. Strain localisation was not detected visually up to the PTP and at  $\gamma_{oct} < 8\%$  in the present study, as can be seen from the photographs in Fig. 20. In the extension tests with  $\alpha_{\sigma'_1} = 90^\circ$  and  $b = 0.5$ , a slight reduction in the outer diameter is observed in the lower portion of the specimen at  $\gamma_{oct} > 8\%$  due to end restraint and stress path effects (Fig. 20c, d); however, this necking is far more well distributed than in the case of  $\alpha_{\sigma'_1} = 90^\circ$  and  $b = 1.0$ , while it is irrelevant to straining near the IP. Thus, the behaviour of specimen A4 presented

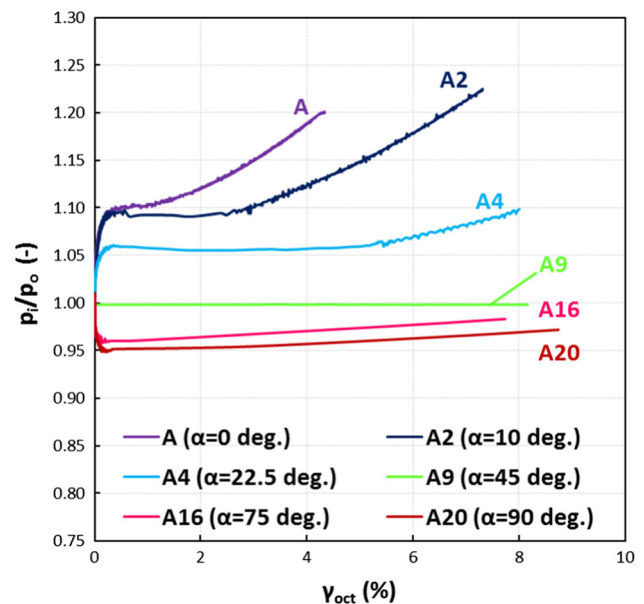


**Fig. 19** Variation of  $p_i/p_o$  with  $\gamma_{oct}$  as an index of stress non-uniformities in A-series tests. The test A is not included in this study

in Fig. 18 is rather not attributed to strain localisation; moreover, most of the failure states in extension-like tests, presented in Fig. 9, were determined before necking.

**Effects of flexible versus stiff boundaries, buckling instability and failure in the  $\sigma_2$ -direction:** It has been shown that the stress–strain non-uniformities at the IP in test A4 are rather minor. However, the slightest

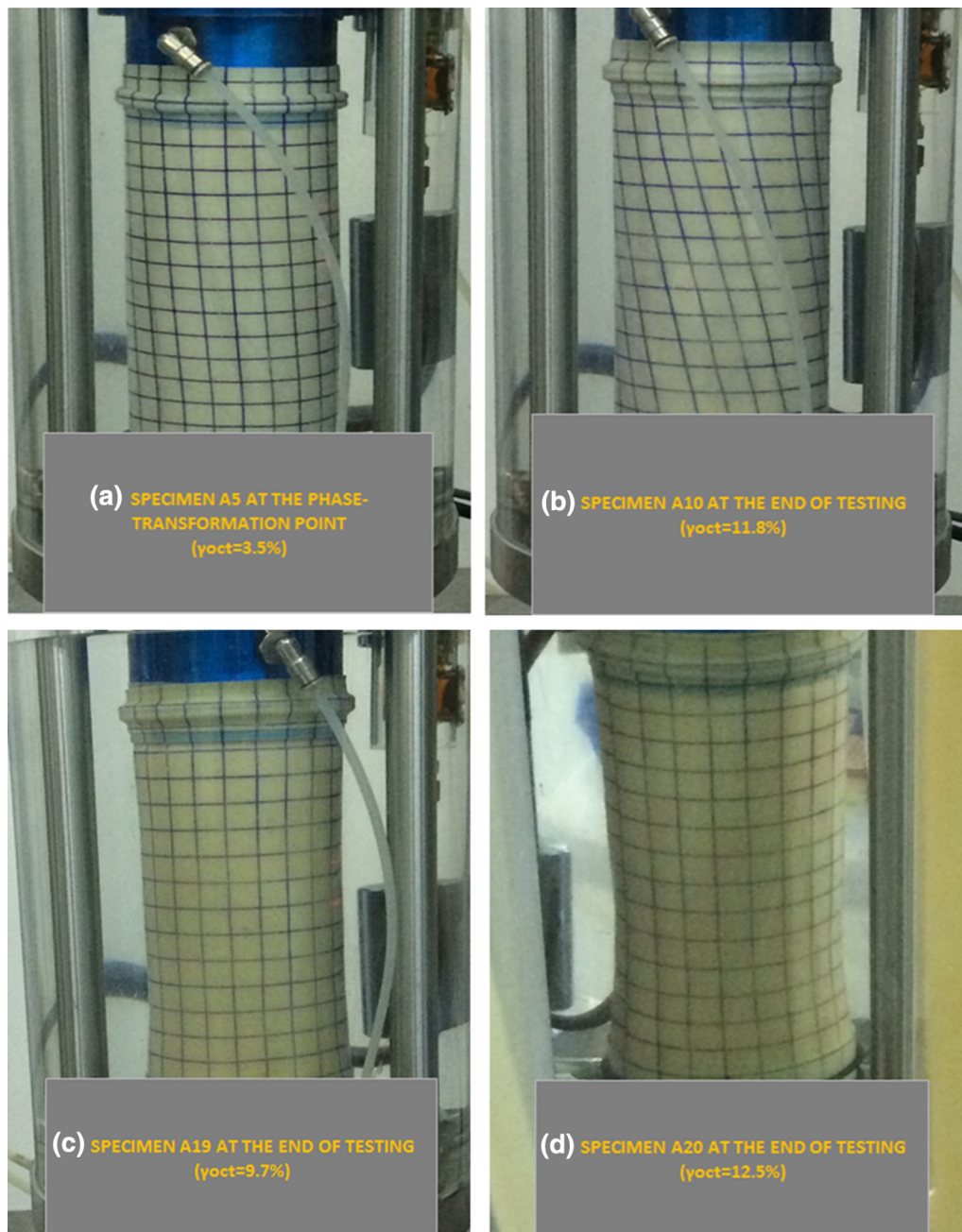


**Fig. 20** Deformation of the specimens in A-series tests at the phase transformation point or at the end of testing. **a** Specimen in test A5 ( $\alpha_{\sigma'1} = 22.5^\circ$ ,  $b = 0.5$ ) at  $\gamma_{\text{oct}} = 3.5\%$ . **b** Specimen in test A10 ( $\alpha_{\sigma'1} = 45^\circ$ ,  $b = 0.5$ ) at  $\gamma_{\text{oct}} = 11.8\%$ . **c** Specimen in test A19 ( $\alpha_{\sigma'1} = 90^\circ$ ,  $b = 0.5$ ) at “ $\gamma_{\text{oct}}$ ” =  $9.7\%$ . **d** Specimen in test A20 ( $\alpha_{\sigma'1} = 90^\circ$ ,  $b = 0.5$ ) at “ $\gamma_{\text{oct}}$ ” =  $12.5\%$ . The photographs were taken under the refraction induced by the crossing of light through the water–perspex–air interfaces

perturbation in the stress–strain field in combination with a minute spatial void-ratio variation may trigger either diffuse or localised bifurcations and induce a progressive development of inhomogeneities. Lade and Rodriguez [40] exposed various instabilities in hollow-cylinder testing of dense sand with  $\alpha_{\sigma'1} = 90^\circ$  and extreme  $b$  values, such as

buckling instabilities and failure in the  $\sigma_2$ -direction, and suggested that “the flexible membranes allow the development of non-uniform strains, shear bands and necking”; they also stated that the stiff boundaries enhance the strength and stiffness of specimens above the values that correspond to the same stress conditions imposed by

flexible boundaries, under homogeneous deformation. None of these severe instabilities was observed before the triggering or after the termination of the bifurcated flow response in test A4; moreover, the stresses  $\tau_{z\theta}$  and  $F/[\pi(r_o^2 - r_i^2)]$  applied by the same stiff boundary were unloaded in a very different way. On the other hand, slight necking was observed at  $\gamma_{\text{oct}} > 8\%$  in tests A14, A16 and A20 (Fig. 4). Since necking occurred in all these tests and the direction of the  $\sigma_1$ -axis is more or less the same regarding the stiff and flexible boundaries (while the  $\sigma_2$ -axis is common), the effect of inherent anisotropy may explain better why the response of specimens A14 and A16 is weaker than that of A20, even at low strains, and why a predisposition to torsional-shear stress unloading is exhibited.

## 6 Conclusions

The undrained behaviour of loose water-pluviated M31 Sand was investigated under generalised loading including principal stress rotation. The results from loading tests at fixed stress directions indicate that the inherent anisotropy affects the strength and deformability of IC sand at the IP, PTP and peak failure state. The results from principal stress rotation tests on AC sand indicate that the combinations of  $\varphi$  and  $\alpha_{\sigma_1}$  at the triggering of flow instability are not unique; thus, the generalised concept of Lade's IL lacks intrinsic value even under the undrained condition. The triggering condition and deformation pattern of flow depend on the stress–strain history, including the effect of  $K_c$  and incremental stress direction; a new flow parameter indicates this dependence. The triggering of both diffuse and localised instabilities occurs preferably at stress states corresponding to unfavourable deformation kinematics, indicating the profound effect of the inherent anisotropy on bifurcation. Nevertheless, the effect of the boundary conditions in hollow-cylinder testing needs further investigation and should not be overlooked.

The novel findings of this study indicate that the stress state of loose sand subjected to undrained principal stress rotation at constant deviatoric stress may move along the direction of isotropic stress unloading from the consolidation state to the failure state without triggering flow. Thereafter, a quasi-static diffuse instability may be triggered on the failure surface under increasing stresses and decreasing stress ratio, followed by a dynamic diffuse instability under decreasing stresses and stress ratio.

**Acknowledgements** The research leading to these results has received funding from the European Research Council under the European Union's Seventh Framework Program FP7-ERC-IDEAS Advanced Grant Agreement no. 290963 with acronym SOMEF.

## References

- Alarcon-Guzman A, Leonards GA, Chameau JL (1988) Undrained monotonic and cyclic strength of sands. *J Geotech Eng* 114(10):1089–1109
- Altuhafi FN, Coop MR, Georgiannou VN (2016) Effect of particle shape on the mechanical behavior of natural sands. *J Geotech Geoenviron Eng*. [https://doi.org/10.1061/\(ASCE\)GT.1943-5606.0001569](https://doi.org/10.1061/(ASCE)GT.1943-5606.0001569)
- Ando E, Hall SA, Viggiani G, Desrues J, Besuelle P (2012) Grain-scale experimental investigation of localised deformation in sand: a discrete particle tracking approach. *Acta Geotech* 7(1):1–13
- Andrade JE, Borja RI (2006) Capturing strain localisation in dense sands with random density. *Int J Numer Meth Eng* 67:1531–1564
- Arthur JRF, Menzies BK (1972) Inherent anisotropy in a sand. *Géotechnique* 22(1):115–129
- Borja RI (2006) Condition for liquefaction instability in fluid-saturated granular soils. *Acta Geotech* 1:211–224
- Castro G (1969) Liquefaction of sands. Harvard Soil Mechanics Series No. 81. Harvard University, Cambridge
- Chen Z, Huang M (2019) Non-coaxial behavior modeling of sands subjected to principal stress rotation. *Acta Geotech*. <https://doi.org/10.1007/s11440-018-0760-4>
- Chu J, Lo S-CR, Lee IK (1992) Strain-softening behavior of granular soil in strain-path testing. *J Geotech Eng* 118(2):191–208
- Chu J, Lo S-CR, Lee IK (1993) Instability of granular soils under strain path testing. *J Geotech Eng* 119(5):874–892
- Chu J, Leong WK (2001) Pre-failure strain softening and pre-failure instability of sand: a comparative study. *Géotechnique* 51(4):311–321
- Dafalias YF, Popov EP (1975) A model of nonlinearly hardening materials for complex loading. *Acta Mech* 21:173–192
- Dafalias YF (1986) Bounding surface plasticity. I: mathematical foundation and hypoplasticity. *J Eng Mech ASCE* 112(9):966–987
- Daouadji A, Darve F, Al Gali H, Hicher PY, Laouafa F, Lignon S, Nicot F, Nova R, Pinheiro M, Prunier F, Sibille L (2011) Wan R (2011) Diffuse failure in geomaterials: experiments, theory and modelling. *Int J Numer Anal Meth Geomech* 35:1731–1773
- Darve F, Flavigny M, Meghachou M (1995) Constitutive modelling and instabilities of soil behaviour. *Comput Geotech* 17(1995):203–224
- Desrues J, Chambon R, Mokni M, Mazerolle F (1996) Void ratio inside shear bands in triaxial sand specimens studied by computed tomography. *Géotechnique* 46(3):529–546
- Desrues J, Viggiani G (2004) Strain localization in sand: an overview of the experimental results obtained in Grenoble using stereophotogrammetry. *Int J Numer Anal Meth Geomech* 28:279–321
- Desrues J, Georgopoulos IO (2006) An investigation of diffuse failure modes in undrained triaxial tests on loose sand. *Soils Found* 46(5):585–594
- Finno RJ, Harris WW, Mooney MA, Viggiani G (1997) Shear bands in plane strain compression of loose sand. *Géotechnique* 47(1):149–165
- Georgiannou VN, Hight DW, Burland JB (1991) Behaviour of clayey sands under undrained cyclic triaxial loading. *Géotechnique* 41(3):383–393
- Georgiannou VN, Tsomokos A, Stavrou K (2008) Monotonic and cyclic behaviour of sand under torsional loading. *Géotechnique* 58(2):113–124

22. Georgiannou VN, Konstadinou M (2014) Torsional shear behavior of anisotropically consolidated sands. *J Geotech Geoenviron Eng ASCE* 140(2):04013017
23. Georgiannou VN, Pavlopoulou E-M, Bikos Z (2017) Mechanical behaviour of sand stabilised with colloidal silica. *Geotech Res* 4(1):1–11
24. Georgiannou VN, Konstadinou M, Triantafyllos P (2018) Sand behavior under stress states involving principal stress rotation. *J Geotech Geoenviron Eng* 144(6):04018028
25. Gong G, Thornton C, Chan AHC (2012) DEM simulations of undrained triaxial behavior of granular material. *J Eng Mech* 138(6):560–566
26. Gudehus G (1979) A comparison for some constitutive laws for soils under radially symmetric loading and unloading. In: Wittke (ed) Third international conference on numerical method. Geomechanics. Balkema Publ., pp 1309–1323
27. Guo N, Zhao J (2013) The signature of shear-induced anisotropy in granular media. *Comput Geotech* 47:1–15
28. Gutierrez M, Ishihara K, Towhata I (1991) Flow theory for sand during rotation of principal stress direction. *Soils Found* 31(4):121–132
29. Hight DW, Gens A, Symes MJ (1983) The development of a new hollow cylinder apparatus for investigating the effects of principal stress rotation in soils. *Géotechnique* 33(4):355–383
30. Hill R (1958) A general theory of uniqueness and stability in elastic-plastic solids. *J Mech Phys Solids* 6:239–249
31. Ishihara K, Tatsuoka F, Yasuda S (1975) Undrained deformation and liquefaction of sand under cyclic stresses. *Soils Found* 15(1):29–44
32. Ishihara K, Towhata I (1983) Sand response to cyclic rotation of principal stress directions as induced by wave loads. *Soils Found* 23(4):11–26
33. Ishihara K (1993) Liquefaction and flow failure during earthquake. *Géotechnique* 43(3):351–415
34. Jiang M, Zhang A, Fu C (2017) 3-D DEM simulations of drained triaxial tests on inherently anisotropic granulates. *Eur J Environ Civ Eng*. <https://doi.org/10.1080/19648189.2017.1385541>
35. Konstantinou M, Georgiannou VN (2013) Cyclic behaviour of loose anisotropically consolidated Ottawa sand under undrained torsional loading. *Géotechnique* 63(13):1144–1158
36. Lade PV, Nelson RB, Ito YM (1988) Instability of granular materials with nonassociated flow. *J Eng Mech* 114(12):2173–2191
37. Lade PV, Pradel D (1990) Instability and plastic flow of soils. I: experimental observations. *J Eng Mech* 116(11):2532–2550
38. Lade PV (1993) Initiation of static instability in the submarine Nerlerk berm. *Can Geotech J* 30:895–904
39. Lade PV, Rodriguez NM, Van Dyck EJ (2014) Effects of principal stress directions on 3D failure conditions in cross-anisotropic sand. *J Geotech Geoenviron Eng* 140(2):04013001
40. Lade PV, Rodriguez NM (2014) Comparison of true triaxial and hollow cylinder tests on cross-anisotropic sand specimens. *Geotech Test J* 37(4):585–596
41. Lam WK, Tatsuoka F (1988) Effects of initial anisotropic fabric and  $\sigma_2$  on strength and deformation characteristics of sand. *Soils Found* 28(1):89–106
42. Lashkari A (2016) Prediction of flow liquefaction instability of clean and silty sands. *Acta Geotech* 11(987–1014):2016
43. Leong WK, Chu J (2002) Effect of undrained creep on instability behaviour of loose sand. *Can Geotech J* 39:1399–1405
44. Li X, Yu H-S (2010) Numerical investigation of granular material behaviour under rotational shear. *Géotechnique* 60(5):381–394
45. Li XS, Dafalias YF (2012) Anisotropic critical state theory: role of fabric. *J Eng Mech* 138(3):263–275
46. Lü X, Huang M, Qian J (2018) Influences of loading direction and intermediate principal stress ratio on the initiation of strain localization in cross-anisotropic sand. *Acta Geotech* 13:619–633
47. Mital U, Andrade JE (2016) Mechanics of origin of flow liquefaction instability under proportional strain triaxial compression. *Acta Geotech* 11:1015–1025
48. Miura K, Miura S, Toki S (1986) Deformation behavior of anisotropic dense sand under principal stress axes rotation. *Soils Found* 26(1):36–52
49. Nakata Y, Hyodo M, Murata H, Yasufuku N (1998) Flow deformation of sands subjected to principal stress rotation. *Soils Found* 38(2):115–128
50. Nicot F, Darve F, Koah H-D-V (2007) Bifurcation and second-order work in geomaterials. *Int J Numer Anal Methods Geomech* 31:1007–1032
51. Nicot F, Darve F (2011) Diffuse and localized failure modes: two competing mechanisms. *Int J Numer Anal Meth Geomech* 35:586–601
52. Nova R (1994) Controllability of the incremental response of soil specimens subjected to arbitrary loading programmes. *J Mech Behav Mater* 5(2):193–201
53. Oda M (1972) Initial fabrics and their relations to mechanical properties of granular material. *Soils Found* 12(1):18–36
54. Oda M, Koishikawa I, Higuchi T (1978) Experimental study of anisotropic shear strength of sand by plane strain test. *Soils Found* 18(1):25–38
55. Oda M, Nemat-Nasser S, Konishi J (1985) Stress-induced anisotropy in granular masses. *Soils Found* 25(3):85–97
56. Papadimitriou AG, Chaloulos YK, Dafalias YF (2019) A fabric-based sand plasticity model with reversal surfaces within anisotropic critical state theory. *Acta Geotech* 14:253–277
57. Poulos SJ, Castro G, France JW (1985) Liquefaction evaluation procedure. *J Geotech Geoenviron Eng* 111(6):772–792
58. Prunier F, Nicot F, Darve F, Laouafa F, Lignon S (2009) Three-dimensional multiscale bifurcation analysis of granular media. *J Eng Mech* 135(6):493–509
59. Roscoe KH, Schofield AN, Wroth CP (1958) On the yielding of soils. *Géotechnique* 8(1):22–53
60. Sasitharan S, Robertson PK, Sego DC, Morgenstern NR (1993) Collapse behavior of sand. *Can Geotech J* 30:569–577
61. Sayao A, Vaid YP (1991) A critical assessment of stress nonuniformities in hollow cylinder test specimens. *Soils Found* 31(1):60–72
62. Schofield AN, Wroth CP (1968) Critical state soil mechanics. McGraw-Hill, London
63. Shibuya S, Hight DW (1987) A bounding surface of granular materials. *Soils Found* 27(4):123–136
64. Shibuya S, Hight DW, Jardine RJ (2003) Four-dimensional local boundary surfaces of an isotropically consolidated loose sand. *Soils Found* 43(2):89–103
65. Shibuya S, Hight DW, Jardine RJ (2003) Local boundary surfaces of a loose sand dependent on consolidation path. *Soils Found* 43(3):85–93
66. Sibille L, Nicot F, Donzé F-V (2007) Darve F (2007) Material instability in granular assemblies from fundamentally different models. *Int J Numer Anal Meth Geomech* 31:457–481
67. Sivathayalan S, Vaid YP (2002) Influence of generalized initial state and principal stress rotation on the undrained response of sands. *Can Geotech J* 39(1):63–76
68. Symes MJ, Gens A, Hight DW (1984) Undrained anisotropy and principal stress rotation in saturated sand. *Géotechnique* 34(1):11–27
69. Tatsuoka F, Sonoda S, Hara K, Fukushima S, Pradhan TBS (1986) Failure and deformation of sand in torsional shear. *Soils Found* 26(4):79–97



70. Tatsuoka F, Sakamoto M, Kawamura T, Fukushima S (1986) Strength and deformation characteristics of sand in plane strain compression at extremely low pressures. *Soils Found* 26(1):65–85
71. Theocharis AI, Vairaktaris E, Dafalias YF, Papadimitriou AG (2017) Proof of incompleteness of Critical State Theory in granular mechanics and its remedy. *J Eng Mech* 143(2):1–12
72. Tian Y (2018) Yao YP (2018) Constitutive modeling of principal stress rotation by considering inherent and induced anisotropy of soils. *Acta Geotech* 13:1299–1311
73. Tong Z, Fu P, Dafalias YF (2014) Yao Y (2014) Discrete element method analysis of non-coaxial flow under rotational shear. *Int J Numer Anal Meth Geomech* 38:1519–1540
74. Vaid YP, Chern JC (1983) Effect of static shear on resistance to liquefaction. *Soils Found* 23(1):47–60
75. Vaid YP, Chung EKF, Kuebris RH (1990) Stress path and steady state. *Can Geotech J* 27:1–7
76. Vaid YP, Sivathayalan S (2000) Fundamental factors affecting liquefaction susceptibility of sands. *Can Geotech J* 37:592–606
77. Vardoulakis I, Sulem J (1995) Bifurcation analysis in geomechanics. Chapman and Hall, London
78. Vardoulakis I, Georgopoulos I-O (2005) The “stress-dilatancy” hypothesis revisited: shear-banding related instabilities. *Soils Found* 45(2):61–76
79. Yamada Y, Ishihara K (1979) Anisotropic deformation characteristics of sand under three dimensional stress conditions. *Soils Found* 19(2):79–94
80. Yamada Y, Ishihara K (1981) Undrained deformation characteristics of loose sand under three-dimensional stress conditions. *Soils Found* 21(1):97–107
81. Yang ZX, Li XS, Yang J (2007) Undrained anisotropy and rotational shear in granular soil. *Géotechnique* 57(4):371–384
82. Yimsiri S, Soga K (2010) DEM analysis of soil fabric effects on behaviour of sand. *Géotechnique* 60(6):483–495
83. Yoshimine M, Ishihara K, Vargas W (1998) Effects of principal stress direction and intermediate principal stress on undrained shear behavior of sand. *Soils Found* 38(3):179–188
84. Yoshimine M, Ishihara K (1998) Flow potential of sand during liquefaction. *Soils Found* 38(3):189–198
85. Zdravković L, Jardine RJ (2001) The effect on anisotropy of rotating the principal stress axes during consolidation. *Géotechnique* 51(1):69–83

**Publisher's Note** Springer Nature remains neutral with regard to jurisdictional claims in published maps and institutional affiliations.